

# Sunyaev-Zel’dovich Cluster Survey Simulations for *Planck*

Jörn Geisbüsch<sup>\*</sup>, Rüdiger Kneissl and Michael Hobson

*Astrophysics Group, Cavendish Laboratory, Madingley Road, Cambridge, CB3 0HE, UK*

30 September 2018

## ABSTRACT

We examine the ability of the future Planck mission to provide a catalogue of galaxy clusters observed via their Sunyaev-Zel’dovich distortion in the cosmic microwave background. For this purpose we produce full-sky Sunyaev-Zel’dovich maps based on N-body simulations and scaling relations between cluster properties for several cosmological models. We extrapolate the N-body simulations by a mass function to high redshifts in order to obtain a realistic SZ background. The simulated Planck observations include, besides the thermal and kinematic Sunyaev-Zel’dovich effects, contributions from the primordial CMB, extragalactic point sources as well as Galactic dust, free-free and synchrotron emission. A harmonic-space maximum-entropy method is used to separate the SZ signal from contaminating components in combination with a cluster detection algorithm based on thresholding and flux integration to identify clusters and to obtain their fluxes. We estimate a survey sensitivity limit (depending on the quality of the recovered cluster flux) and provide cluster survey completeness and purity estimates. We find that given our modelling and detection algorithm Planck will reliably detect at least several thousands of clusters over the full sky. The exact number depends on the particular cosmological model (up to 10000 cluster detections in a concordance  $\Lambda$ CDM model with  $\sigma_8 = 0.9$ ). We show that the Galaxy does not significantly affect the cluster detection. Furthermore, the dependence of the thermal SZ power spectrum on the matter variance on scales of  $8 h^{-1}$  Mpc and the quality of its reconstruction by the employed method are investigated. Our simulations suggest that the Planck cluster sample will not only be useful as a basis for follow-up observations, but also will have the ability to provide constraints on cosmological parameters.

**Key words:** cosmology: large-scale structure of the Universe – cosmology: cosmic microwave background – cosmology: theory – methods: data analysis – methods: statistical.

## 1 INTRODUCTION

In addition to measuring primordial CMB fluctuations, the Planck Surveyor satellite, which is scheduled for launch in 2007, will have the ability to construct a cluster catalogue via the Sunyaev-Zel’dovich (SZ) effect (Sunyaev & Zel’dovich 1972; Sunyaev & Zel’dovich 1980; recent reviews: Rephaeli 1995; Birkinshaw 1999; Carlstrom, Holder, & Reese 2002). Since Planck will provide detailed full-sky maps at nine different frequencies, ranging from 30 to 850 GHz, it is a particularly suitable instrument to detect the thermal SZ effect of galaxy clusters owing to its distinctive frequency dependence. Moreover, since the SZ effect is redshift independent and clusters – as the most massive collapsed objects in the universe – are tracers of the underlying linear matter density perturbations, their observation provides a unique

tool for studying large scale structure and constraining cosmological parameters.

In this work we investigate the yield, completeness and purity of such a Planck SZ survey for a range of cosmological models and estimate the cosmological significance of such the resulting cluster catalogue. Furthermore, based on our simulations and cluster selection we estimate a Planck cluster survey flux limit and provide tabulated cluster number counts for each model. In contrast to previous work (Kay, Liddle, & Thomas 2001; Diego et al. 2002; White 2003), which studied the cluster sample either on sky patches or neglected contaminants, we perform full-sky simulations including all known significant extragalactic and Galactic contaminating components. Our modelling of the SZ effect as well as contaminants aims to be as realistic as current observational constraints allow. To recover the SZ signal of single clusters we make use of the harmonic-space maximum entropy method introduced by Stolyarov et al. (2002) in combination with a cluster finding algorithm based on

<sup>\*</sup> email: joern@mrao.cam.ac.uk

peak detection, thresholding and flux integration. As Stolyarov et al. (2002) show the HSMEM is a novel method to separate various CMB components. The cluster finding algorithm is shown in this paper to be able to obtain reliable flux as well as radius estimates for a cluster sample above the estimated survey flux limit. Note that besides the assumed cosmological model the cluster recovery algorithm has major implications on the number of clusters obtained by the Planck survey and thus its impact on constraining cosmological parameters. It is therefore important to explore, improve and combine techniques in order to find the optimal method and maximise the survey yield. Since our modelling exhibits a high degree of realism, the given estimate of the cluster number which can be obtained by the Planck survey using our algorithm is reliable. Even though further improvement is possible, the presented combined cluster detection method – as we show below – provides already the quality to draw interesting cosmological conclusions from the obtained cluster sample.

The outline of the paper is as follows. In section 2 a short introduction to the SZ effect is given. The modelling of full-sky SZ maps of different cosmological models and of the contaminants is described in section 3. Moreover, section 3 contains a brief description of how Planck observation simulations are obtained from the modelled components. In section 4, the applied reconstruction method used to recover the fluxes of single galaxy clusters is explained. Section 5 contains a presentation and discussion of the results. Finally, a summary and conclusions are given in section 6.

## 2 THE SUNYAEV-ZEL'DOVICH EFFECT

The CMB anisotropy caused by the SZ effect can be separated into two contributions which are distinguished by the origin of energy of the scattering electrons that is responsible for the shift of photon frequency. The total CMB distortion due to the SZ effect is given by

$$\frac{\Delta I_\nu}{I_0} = g(x)y - h(x)\beta\tau, \quad (1)$$

where  $x = h\nu/k_B T_0$  with  $T_0 = 2.725$  K (Mather et al. 1999) and  $I_0 = 2k_B^3 T_0^3/h^2 c^2$ . The first term in equation (1) is the so called thermal SZ effect due to the thermal motion of electrons of the intra-cluster gas. The thermal SZ effect has a spectral shape given by

$$g(x) = \frac{x^4 e^x}{(e^x - 1)^2} \left[ x \frac{e^x + 1}{e^x - 1} - 4 \right], \quad (2)$$

and a frequency independent magnitude, the Comptonization parameter,

$$y = \frac{k_B \sigma_T}{m_e c^2} \int n_e T_e dl. \quad (3)$$

In hot clusters ( $T_e > 5$  keV) the relativistic electrons present slightly modify the spectral shape of the thermal SZ effect (Challinor & Lasenby 1998). This resulting relativistic correction has not been taken into account in this work, since its effect on the results presented is negligible. The detectability of the effect from thermal (e.g. Pointecouteau et al. 1998) and non-thermal (e.g. Ensslin & Hansen 2004) relativistic

Model	$\Omega_0$	$\Omega_\Lambda$	$h$	$\Gamma$	$\sigma_8$	$m/10^{12} h^{-1} M_\odot$
$\tau$ CDM	1.0	0.0	0.5	0.21	0.6	2.22
$\Lambda$ CDM	0.3	0.7	0.7	0.21	0.9	2.25

**Table 1.** Key parameters of the Hubble Volume simulations.  $\Omega_0$  is the density parameter,  $\Omega_\Lambda \equiv \Lambda/3H_0^2$  the cosmological constant,  $h \equiv H_0/100 \text{ km s}^{-1} \text{ Mpc}^{-1}$  the Hubble constant,  $\Gamma$  the power spectrum shape parameter,  $\sigma_8$  the variance of linear fluctuations smoothed with a top-hat filter on the (comoving) scale of  $8 h^{-1} \text{ Mpc}$  at  $z = 0$  and  $m$  the N-body particle mass.

electrons has been estimated. The spectral shape of the second contribution in equation (1), the kinematic SZ effect, is given by

$$h(x) = \frac{x^4 e^x}{(e^x - 1)^2}, \quad (4)$$

and its magnitude,  $\beta = v_{\text{pec}}/c$ , depends on the uniform peculiar line-of-sight bulk motion of the cluster's electron plasma,  $v_{\text{pec}}$ .

$$\tau = \sigma_T \int n_e dl, \quad (5)$$

is the Thomson optical depth. In the case the cluster can be assumed to be isothermal the Comptonization parameter can be expressed by

$$y = \left( \frac{k_B T_e}{m_e c^2} \right) \tau. \quad (6)$$

In this paper we concentrate on the thermal SZ effect and treat the kinematic merely as a contaminant to the thermal SZ.

## 3 SIMULATING THE SUNYAEV-ZEL'DOVICH EFFECT ON THE FULL SKY

### 3.1 The cluster halo distribution

There are two possible ways to obtain the distribution of cluster halos in redshift space. The first one is based on assuming a cluster mass function (see e.g. Press & Schechter (1974); Sheth & Tormen (1999); Jenkins et al. (2001); Evrard et al. (2002) for cluster mass functions). This approach determines the number of clusters within a given mass range at redshift  $z$  per comoving volume element,

$$\frac{dN}{dz} = \Delta\Omega \frac{dV}{dz d\Omega}(z) \int_{M_{\text{lim}}}^{\infty} \frac{dn(M, z)}{dM} dM, \quad (7)$$

where  $dV/(dz d\Omega)$  is the comoving volume element and  $(dn/dM)dM$  is the comoving density of clusters of mass  $M$ .

The second approach is based on performing N-body simulations and extracting halos from them to obtain halo catalogues which include halo masses, three-dimensional positions and the halo three-dimensional velocities. Such catalogues have been obtained by applying a spherical overdensity algorithm for the ‘Hubble volume’ simulations (see Frenk et al. 2000), the largest N-body simulations yet performed. Since, besides the halo redshift distribution, N-body simulations also provide information about halo clustering and dynamics, we decided to utilise these N-body simulations. These simulations investigate structure formation in two cosmologies, a  $\tau$ CDM and  $\Lambda$ CDM model. They provide

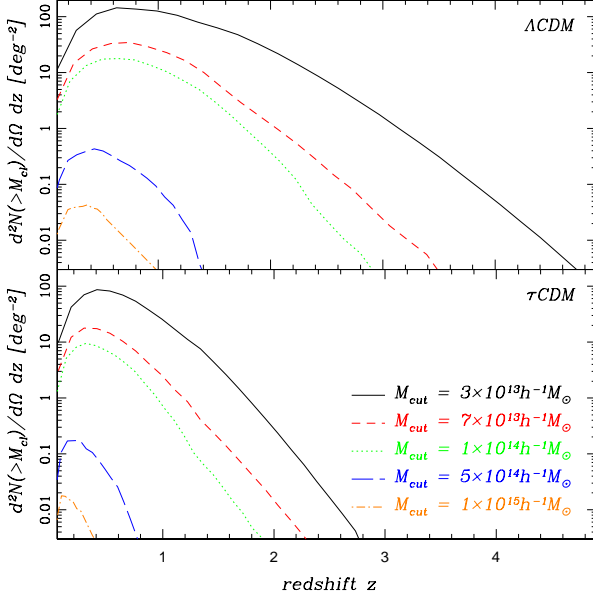


**Figure 1.** The cosmology dependent differential surface cluster number count per redshift bin  $\Delta z = 1$  for different lower cluster mass limits. The upper panel shows the number counts obtained from the fiducial  $\Lambda$ CDM simulation and the lower panel the ones for fiducial  $\tau$ CDM model (see Table 1). A typical cluster detected by Planck has a mass of approximately  $5 \times 10^{14} h^{-1} M_{\odot}$ . The lower mass clusters provide a realistic cluster-cluster confusion noise.

halo catalogues of lightcone datasets for a sphere, two octants and a wedge for each cosmological model (see Table 1). To obtain a full-sky realisation of the SZ effect we make use of the sphere and octant datasets. Nevertheless, especially in the case of the  $\Lambda$ CDM model, the redshift cut-off of even the octants ( $z \approx 1.5$ ) is rather low, since objects of intermediate masses ( $M \approx 1 \times 10^{14} h^{-1} M_{\odot}$  and below) exist at higher redshift. These objects contribute significantly to the background cluster confusion, given the  $\Lambda$ CDM cluster redshift distribution (see Figure 1). Therefore we extend the N-body simulations to higher redshifts by using a mass function to obtain the differential number density,

$$\frac{dn}{d\ln M}(M, z) = -A \frac{\rho_m}{M} \frac{d\ln \sigma(M)}{d\ln M} \times \exp\{-|B - \ln[g(z)\sigma(M)]|^{\epsilon}\}, \quad (8)$$

whose calibration has been directly derived from the Hubble volume (HV) simulations (Evrard et al. 2002) and is thus consistent. These extra high redshift halos due to the extension of the simulations are mainly added to provide a realistic SZ background confusion. In equation (8),  $\rho_m = \Omega_m(0)3H_0^2/(8\pi G)$  is the present mass density,  $\sigma(M)$  the variance of the density field smoothed with a spherical top-hat filter enclosing mass  $M$  at the mean density and  $g(z)$  is the linear growth factor normalised to  $g(0) = 1$ . In the case of the  $\Lambda$ CDM model Evrard et al. (2002) find the best fit mass function parameters to the HV simulations to be  $A = 0.22$ ,  $B = 0.73$  and  $\epsilon = 3.86$  and for the  $\tau$ CDM cosmology  $A = 0.27$ ,  $B = 0.65$  and  $\epsilon = 3.77$ .

### 3.2 Halo properties from scaling relations

Besides the mass of the dark matter halo, which is directly obtained from the N-body simulations, further cluster properties, such as the electron gas temperature  $T_e$  and virial radius  $r_v$ , are needed in order to model the SZ effect of galaxy clusters.

#### 3.2.1 The mass-temperature relation

Assuming that clusters are self-similar, virialised and isothermal, the mass-temperature (M-T) relation can be derived analytically (Kaiser 1986) and takes the form:

$$\frac{M_{cl}}{10^{15} h^{-1} M_{\odot}} = \left[ \frac{\beta}{(1+z)(\Omega_m \Delta_c / \Omega_m(z))^{1/3}} \frac{T_e}{\text{keV}} \right]^{3/2}, \quad (9)$$

where  $M_{cl}$  is the mass of the cluster within its virial radius,  $\Delta_c$  is the mean overdensity inside the virial radius in units of critical density and  $\beta$  parameterises the scaling relation. In general,  $\beta$  may be a function of  $T_e$  as well as cosmology and redshift. In the case of a flat cosmology ( $\Omega_{\Lambda} + \Omega_m = 1$ )

$$\Delta_c \approx 18\pi^2 + 82(\Omega_m(z) - 1) - 39(\Omega_m(z) - 1)^2 \quad (10)$$

(Eke et al. 1996). While in theory  $\beta \approx 0.75^1$  and is therefore independent of  $T_e$  and cosmology, this result, which has also been found by numerical simulations (see Pierpaoli et al. 2001, for a listing of results), differs from the ones obtained by observations which favour lower normalisations, i.e.  $\beta \approx 0.54(T_{ew}/6\text{keV})^{0.24}$ , where  $T_{ew}$  is the emission-weighted X-ray temperature of the intracluster gas. This observational normalisation has been derived from Finoguenov et al. (2001) by converting the mass at a mean overdensity of 500 times the critical density to the virial cluster mass (see Hu & Kravtsov 2003). Note that the findings of Finoguenov et al. (2001) are in good agreement with Allen et al. (2001). To do the conversion, it has been assumed that the dark matter distribution, which constitutes most of the cluster mass, obeys a NFW profile, since CDM is the major cluster mass component and simulations show that its distribution is well described by the NFW profile (see e.g. Navarro et al. 1997). Although there has been some controversy, this assumption is supported by observations. For example, by testing different dark matter models against mass profiles derived from an XMM-Newton observation of the relaxed cluster A478 under the hypothesis of hydrostatic equilibrium, Pointecouteau et al. (2004) find that the NFW profile is significantly preferred to other models. To distribute intracluster electron gas, however, we use a  $\beta$ -model. This assumption is supported by X-ray observations of relaxed galaxy clusters (see e.g. Ettori et al. 2004). In the case of isothermality and hydrostatic equilibrium it has been shown that the expected gas profile of a NFW dark matter halo is well approximated by such a  $\beta$ -profile (Eke, Navarro & Frenk 1998). Note further, that in the case of isothermality,  $T_e = T_{ew}$ , the observational result predicts a lower mass at fixed  $T_e$  than is predicted by theory. The assumption that clusters are isothermal is in good agreement with recent XMM-Newton observations of outer

<sup>1</sup> Note that the theoretical prediction is based on a number of assumptions, such as hydrostatic isothermality of the cluster and  $\beta$ -profile adherence of the cluster gas (see e.g. Sarazin 1986).

cluster regions which find that the cluster temperature profiles are isothermal within  $\pm 10$  per cent up to approximately half the virial radius (Arnaud et al. 2003).

In the following we will use both normalisations of the M-T relation, the observed as well as the theoretical one, to analyse the difference it makes and if a Planck SZ survey will be able to distinguish between them.

### 3.2.2 The integrated Comptonization parameter $Y$ and the total cluster flux density $S_\nu$

After specifying the cluster abundance and the mass-temperature relation, we relate the observable flux due to the thermal SZ effect to the cluster mass. Since the spectral behaviour of the thermal SZ effect is the same for all clusters (see equation 2), the total SZ flux density can be expressed in terms of the integrated Comptonization parameter

$$Y = r_d^{-2} \int y dA, \quad (11)$$

where  $d\Omega = dA/r_d^2$ ,  $r_d$  is the angular diameter distance to the galaxy cluster and one integrates over the cluster's projected area. Then the total flux density  $S_\nu$  at frequency  $\nu$ , which is usually given in units of Jy, is

$$S_\nu(x) = \frac{x^4 e^x}{(e^x - 1)^2} \left[ x \frac{e^x + 1}{e^x - 1} - 4 \right] Y = g(x)Y, \quad (12)$$

where again  $x = h\nu/k_B T_0$ .

In our case, where we assume the cluster to be isothermal, the integrated Comptonization parameter is further given by

$$\begin{aligned} Y &= \frac{k_B \sigma_T}{m_e c^2} r_d^{-2} T_e \left[ \int \left( \int n_e dl \right) dA \right] \\ &= \frac{k_B \sigma_T}{m_e c^2} r_d^{-2} T_e N_e, \end{aligned} \quad (13)$$

where we have used equation (6), and  $N_e$  the total number of thermal electrons within the cluster. The total number of electrons within a cluster's virial radius is proportional to the virial mass of the cluster,

$$N_e = \left( \frac{1 + f_H}{2m_p} \right) f_{gas} M_{cl}, \quad (14)$$

where  $f_{gas}$  is the baryonic gas mass fraction of the total cluster mass,  $f_H$  is the hydrogen fraction of the baryonic mass – in the following we assume  $f_H = 0.76$  – and  $m_p$  is the proton mass. Therefore, the integrated Comptonization parameter  $Y$ , or respectively the total flux density, of the cluster can be related to the cluster's virial mass by

$$\begin{aligned} Y &= \frac{k_B \sigma_T}{m_e c^2} r_d^{-2} T_e \left( \frac{1 + f_H}{2m_p} \right) f_{gas} M_{cl} \\ &= 0.1 \times (1 + f_H) f_{gas} \left( \frac{T_e}{\text{keV}} \right) \left( \frac{M_{cl}}{10^{15} h^{-1} M_\odot} \right) \\ &\quad \times \left( \frac{r_d}{100 h^{-1} \text{Mpc}} \right)^{-2} h \text{ arcmin}^{-2} \\ &= 0.1 \times (1 + f_H) f_{gas} \beta^{-1} (1 + z) \\ &\quad \times \left( \frac{\Delta_c \Omega_m}{\Omega_m(z)} \right)^{1/3} \left( \frac{M_{cl}}{10^{15} h^{-1} M_\odot} \right)^{5/3} \end{aligned}$$

$$\times \left( \frac{r_d}{100 h^{-1} \text{Mpc}} \right)^{-2} h \text{ arcmin}^{-2}. \quad (15)$$

Hence, apart from the normalisation,  $Y$  depends on the cluster gas mass, the cosmology and the cluster redshift.

### 3.2.3 The cluster electron gas density profile

Since the  $\beta$ -model has been empirically found to fit well the electron gas density profile obtained from X-ray observations, and since most of the clusters will be unresolved given the resolutions of the Planck channels (see section 3.5.6), we utilise a spherical isothermal  $\beta$ -profile,

$$\rho(r) = \rho_0 \left[ 1 + \left( \frac{r}{r_c} \right)^2 \right]^{-3/2\beta_{\text{prof}}}, \quad (16)$$

to model the electron gas distribution inside the cluster's virial radius. The line-of-sight projected  $\beta$ -profile is given by:

$$n_e^{\text{proj}}(r) = n_{e0} \left[ 1 + \left( \frac{r}{r_c} \right)^2 \right]^{1/2 - 3/2\beta_{\text{prof}}}, \quad (17)$$

where  $r_c$  is the cluster core radius and  $n_{e0}$  is the central electron gas density. For our simulations we make the common choice of  $\beta_{\text{prof}} = 2/3$ . While this choice of  $\beta$  is consistent with the assumption of hydrostatic equilibrium for the virial M-T relation normalisation, for the one derived from X-ray observations the resulting cluster  $y$ -profile given the gas density mimics a temperature gradient. When a truncation of the cluster electron gas profile (16) is performed at the virial radius, the projected profile becomes

$$n_e^{\text{proj}}(r) = \frac{2n_{e0}}{\sqrt{1 + (r/r_c)^2}} \times \arctan \sqrt{\frac{b^2 - (r/r_c)^2}{1 + (r/r_c)^2}}, \quad (18)$$

where  $b$  relates the cluster core radius to the virial radius (see below). This truncation ensures that the cluster SZ signal drops to zero within a finite range from the cluster centre. Thus, in the cluster outskirts the projected profile (18) declines more rapidly than the one given by (17). The resulting change in the shape of the projected profile also agrees better with predictions obtained from hydrodynamical simulations.

As mentioned above, we use the virial radius to define the edge of the cluster. Since  $M_{cl} = \frac{4}{3}\pi\bar{\rho}r_v^3$ , where  $\bar{\rho}$  is the mean matter density inside  $r_v$ , the virial radius of the cluster is given by:

$$\begin{aligned} r_v &= 2.12 \times \left( \frac{M_{cl}}{10^{15} h^{-1} M_\odot} \right)^{1/3} (1 + z)^{-1} \\ &\quad \times \left( \frac{\Omega_m \Delta_c}{\Omega_m(z)} \right)^{-1/3} h^{-1} \text{Mpc}. \end{aligned} \quad (19)$$

Moreover, we relate the cluster core radius  $r_c$  to its virial radius  $r_v$  by  $r_c(z) = b(z)r_v$ , where  $b(z=0) \approx 0.14$  and the evolution of the cluster profile can be described by:

$$r_c(z) = r_c(z=0) \times (1 + z)^{1/5}. \quad (20)$$

The scaling  $b(z)$  has been chosen so that the evolution of the central electron density of the cluster  $n_{e0}$  is consistent with simulations (see e.g. Eke et al. (1998)).

Given the shape of the electron gas density profile, the electron gas distribution and therefore the optical depth can be normalised in terms of the cluster's virial mass by utilising equations (14) and (16) and by making use of

$$\int_0^{r_v} \rho_{gas}(r) 4\pi r^2 dr = f_{gas} M_{cl}. \quad (21)$$

Hence, one deduces that the central electron gas density is given by:

$$n_{e0} = 1.6 \times 10^3 h^2 f_{gas} \left( \frac{1 + f_H}{w} \right) \left( \frac{r_c}{h^{-1} \text{Mpc}} \right)^{-3} \left( \frac{M_{cl}}{10^{15} h^{-1} M_\odot} \right) \text{m}^{-3}, \quad (22)$$

where  $w$  is given by

$$w = b^{-1} + \arctan(b) - \frac{\pi}{2} \quad (23)$$

when we assume a  $\beta$ -profile with  $\beta_{\text{prof}} = 2/3$ . Note that – besides the relation for the central electron gas density – all scaling relations between cluster properties, which are given above, are independent of the chosen electron gas profile.

Since the scaling relations presented above are for virial cluster properties, we have to rescale the cluster masses given by the Hubble volume cluster catalogues and the mass function of Evrard et al. (2002), as they provide the cluster mass within a radius for which the mean density contrast  $\Delta_c = 200$ . The cluster mass rescaling is discussed in section 3.4.

### 3.3 Varying $\sigma_8$

In order to rescale the cluster halo dark matter masses to values of  $\sigma_8$  which differ from the default  $\sigma_8$  used in the conducted HV N-body simulations we follow the formalism presented in Evrard et al. (2002). A relation between the change in  $\sigma_8$ ,  $\Delta\sigma_8$ , and the related change in cluster mass,  $\Delta M$ , can be derived by setting to zero the total derivative of the differential comoving cluster number density (equation 8) at fixed redshift  $z$ . The resulting relation is given by

$$\frac{\Delta\sigma_8}{\sigma_8} = \alpha'(M) \frac{\Delta M}{M} \quad (24)$$

with

$$\alpha'(M) = \alpha_{\text{eff}}(M) + \frac{(1 - 2b/\alpha_{\text{eff}}(M))}{\epsilon (\ln\sigma^{-1}(M) + B)^{\epsilon-1}} \quad (25)$$

where  $\alpha_{\text{eff}}(M) \equiv d\ln\sigma^{-1}(M)/d\ln M$  and can be obtained by employing the quadratic relation describing the filtered power spectrum shape given in Evrard et al. (2002). As has been pointed out by Evrard et al. (2002), the number of the rarest most massive clusters is most sensitive to a change in  $\sigma_8$ .

This expression (equation 25) differs from the one in Evrard et al. (2002), since we do not make any approximation. In particular, for lower masses this expression is slightly more accurate (10 per cent for  $M_{cl} = 1 \times 10^{14} h^{-1} M_\odot$ ). The presented rescaling relation between the halo dark matter mass and the change in  $\sigma_8$  has been used to convert the CDM cluster masses of the fiducial HV simulations (see Table 1) to the ones of models with different values of  $\sigma_8$ , a still rather unconstrained parameter by today's observation.

### 3.4 Converting to virial mass

Commonly, a cluster halo is defined to be a spherical overdense region – in the case of N-body simulations – of particles, whose internal mean density,  $\langle\rho\rangle$ , is given as a multiple either of the critical density  $\rho_c(z) = 3H(z)^2/8\pi G$  or of the overall mean matter density  $\bar{\rho}(z) = \Omega_m(z)\rho_c(z)$ . For the HV catalogues  $\Delta_c = 200$ , where  $\langle\rho\rangle = \Delta_c\rho_c(z)$ . In the case of the  $\tau$ CDM model this is not far-off the prediction of  $\Delta_c \approx 178$  given by the spherical top-hat collapse model for a sphere that encloses the virial mass,  $M_{cl}$  (see Lacey & Cole (1993)). For the fiducial  $\Lambda$ CDM cosmology however this value differs approximately by a factor of two from the predicted collapse model value of  $\Delta_c(0) \approx 103$  at redshift  $z = 0$ , and  $\Delta_{\bar{\rho}}(0) \approx 667$  for the HV simulations. Since the scaling relations presented above, especially the M-T relation (see equation 9), are derived for the virial cluster properties, either the cluster mass has to be directly converted to yield the virial mass of the cluster or one has to rescale the relations by deriving an approximate formula to the cluster mass conversion. Note, in either case a halo density profile has to be assumed in order to be able to convert various definitions of the cluster mass into each other.

Therefore, in this paper we proceed by assuming a NFW halo profile of the dark matter which contributes mainly to the total cluster mass and follow the recipe as it has been suggested in Hu & Kravtsov (2003) to rescale the dark matter halo masses.

### 3.5 Simulating Planck Observations

The thermal and kinematic SZ effect contributions to a full-sky map at each Planck channel are obtained from catalogues of cluster properties by employing the relations and profile discussed above. Further components regarded as contamination of the clusters' SZ signal were also simulated. The following paragraphs contain short descriptions of the realisation of these further components.

#### 3.5.1 Primordial CMB

The realizations of full-sky maps of the primordial CMB for different cosmological models are generated by assuming that the primordial CMB is a homogeneous random Gaussian field entirely described by a standard CDM power spectrum whose shape and normalisation agrees with WMAP measurements (Bennett et al. 2003). The  $C_l$  coefficients have been created using CAMB (Lewis, Challinor & Lasenby 2000).

#### 3.5.2 Point sources

Point source contamination has been included in our simulations. Here we follow the modelling approach presented in Hobson et al. (1999). In respect of the component reconstruction, which is performed in spherical harmonics space (see section 4.1), we make the assumption that the point source contribution in each Planck frequency channel should be well modelled as random Gaussian noise in the Fourier or spherical harmonics domain. The contribution by the point source population is determined by number counts predicted by Toffolatti et al. (1998) based on the evolution model of

Instrument	LFI			HFI					
Central frequency (GHz)	30	44	70	100	143	217	353	545	857
Angular resolution (FWHM, arcmin)	33	24	14	9.2	7.1	5	5	5	5
Sensitivity per pixel ( $\mu K$ ) (after three full sky coverages)	4.5	6	10.5	4.5	4.9	10.7	32.7	327.7	14935

**Table 2.** Basic observational characteristics of the 9 frequency channels of the Planck instruments (Low Frequency Instrument (LFI) and High Frequency Instrument (HFI)). The angular resolutions are quoted as FWHM for a Gaussian beam. The sensitivities quoted will be achieved by Planck after three full sky coverages. A pixel is a square whose side is the FWHM extent of the beam.

radio sources of Danese et al. (1987) and the far-IR source evolution model by Franceschini et al. (1994), which has been updated by Burigana et al. (1997) to account for an isotropic sub-mm component. The rms thermodynamic temperature fluctuation within a defined pixel area due to the point source population in each Planck channel after beam-convolution is shown in Figure 4 of Hobson et al. (1999) for sources in the  $10^{-5}\text{Jy} < S(\nu) < 10\text{Jy}$  flux range. We assume no correlation of the point sources with each other or with clusters of galaxies. In the case of radio point sources however it is known that they have in fact a correlation with galaxy clusters. Thus, our assumption leads to some underestimate of confusion at the lowest Planck frequencies. If IR sources originate at high redshift ( $z > 3$ ) as suggested by current models as well as SCUBA observations at  $850\text{-}\mu\text{m}$  (Holland et al. 1998; Smail et al. 1998; Blain et al. 1998), the assumption of IR sources being uncorrelated with clusters which are detectable by Planck (see section 5.2) is valid. Generally, the contribution of clustered sources is found to be small in comparison to the Poisson term. Note that the Toffolatti model has been found to agree within a factor of two with results obtained from the WMAP mission (Bennett et al. 2003). The WMAP results suggest that the model actually overpredicts the point source contribution. This is also supported by recent VSA 9C survey counts (see Figure 13 in Bennett et al. 2003). Thus, our modelling is rather pessimistic concerning the radio point source contribution. IR sources are expected to dominate the number counts of bright objects at frequencies  $\nu > 100\text{ GHz}$ , whereas radio sources are a significant contaminant below  $\nu = 100\text{ GHz}$ . Currently the best observational limits on the IR source contribution are obtained from SCUBA. These observations suggest that the IR source contribution could be up to a few times higher than predicted by the Toffolatti model at  $353\text{ GHz}$ . However, since the SCUBA surveyed area is rather small (a few  $10\text{ arcmin}^2$ ) and IR sources relevant to Planck are at the bright end of the SCUBA population, the sample variance is quite large and does not yield any final conclusions about the IR source contribution.

### 3.5.3 Galactic dust emission

The dust emission is modelled using the DIRBE-IRAS  $100\text{-}\mu\text{m}$  dust map (Schlegel, Finkbeiner & Davis 1998). Its resolution of  $5\text{ arcmin}$  is sufficient for our modelling purpose since it is comparable to the high frequency channel resolutions of Planck. To extrapolate the flux at  $100\text{-}\mu\text{m}$  to the Planck observing frequencies a one-component dust model

with a temperature of  $T_{\text{dust}} = 18\text{K}$  and a dust emissivity  $\beta = 2$  is assumed by taking into account the colour correction of the DIRBE  $100\text{-}\mu\text{m}$  filter.

### 3.5.4 Galactic synchrotron emission

The destriped version of the  $408\text{MHz}$  Haslam survey (Haslam et al. 1982), to which artificial substructure on sub-degree scale has been added by extrapolating the power spectrum, is used as the synchrotron emission template. Its extrapolation to  $300\text{ GHz}$  has been obtained by using an all-sky spectral index map derived from low frequency surveys at  $408\text{ MHz}$ ,  $1420\text{ MHz}$  (Reich & Reich 1986) and  $2326\text{ MHz}$  (Jonas, Baart & Nicholson 1998) and padding the unobserved area around the South pole with the mean spectral index. By assuming a constant spectral index  $\beta = 0.9$  the synchrotron emission at the Planck channel frequencies has been predicted.

### 3.5.5 Galactic free-free emission

A full-sky free-free emission template has been created on the basis of the DIRBE/IRAS dust map. 60 per cent of the free-free emission is assumed to be dust correlated. The dust uncorrelated free-free component has been obtained by flipping the dust map north-south in Galactic coordinates. A spectral index of  $\beta = -0.16$  has been assumed and the normalisation has been taken from Bouchet & Gispert (1999).

### 3.5.6 Planck channel observations

Realistic Planck surveyor simulations are then obtained at each of the  $n_f = 9$  observing frequencies (see Table 2) along the line-of-sight  $\hat{x}$  by summing up the contributions of the physical components along this direction, convolving the resulting anisotropy map with the Planck beam at each particular frequency and adding the channel noise, which is assumed to be uncorrelated and Gaussian. This can be conveniently represented as a data vector of length  $n_f$  containing the resulting observing signal in direction  $\hat{x}$  at each frequency:

$$d_\nu(\hat{x}) = \int_{4\pi} B_\nu(\hat{x} \cdot \hat{x}') \sum_{p=1}^{n_c} F_{\nu p} s_p(\hat{x}') d\Omega' + \epsilon_\nu(\hat{x}), \quad (26)$$

where  $F_{\nu p} = \int_0^\infty t_\nu(\nu') f_p(\nu') d\nu'$  is the frequency response matrix,  $B_\nu$  is the beam profile of the  $\nu$ th frequency channel.

Up-to-date beam sizes and instrumental channel noises for Planck are given on the Planck homepage<sup>2</sup>.

In order to reduce the instrumental noise contribution in the high-frequency Planck channels to a level comparable to the point source noise, the presented results have been obtained by simulating Planck observations of one and a half year duration (approximately three full sky coverages).

Even more realistically one expects anisotropic instrumental noise and spatial variations of the Galactic dust temperature and spectral index. Stolyarov et al. (2004) have recently extended their modelling to accommodate these effects and applied the HSMEM to the simulated Planck channel observations. Since they find that these spatial variations do not affect the recovery quality of the components, our modelling is sufficient to obtain reliable results. In any case, these variations happen on scales larger than the typical cluster scale and thus the assumption of locally constant noise and foreground properties in cluster-sized regions is a reasonable one.

## 4 RECONSTRUCTING CLUSTER'S SZ SIGNAL

### 4.1 The HSMEM

In order to extract the thermal SZ signal from other CMB components on the sky, we use the harmonic-space maximum entropy method (HSMEM) as presented in Stolyarov et al. (2002). This method allows us to perform a full-sky separation of all input components described above in spherical harmonic space. While the HSMEM has been developed mainly focusing on the recovery of the primordial CMB component and its power spectrum, it has been applied in this work to extract the thermal SZ component and all other components have been considered as contaminating noise. In the following a short description of the method is presented. A detailed explanation of the method can be found in Stolyarov et al. (2002) and Hobson et al. (1998).

The HSMEM is a Bayesian method. In the spherical harmonic representation when we neglect any coupling between different  $(l, m)$  modes, the posterior distribution, which we want to explore, is given by

$$\Pr(\mathbf{a}_{\ell m} | \mathbf{D}_{\ell m}) \propto \Pr(\mathbf{D}_{\ell m} | \mathbf{a}_{\ell m}) \Pr(\mathbf{a}_{\ell m}), \quad (27)$$

where  $\Pr(\mathbf{D}_{\ell m} | \mathbf{a}_{\ell m})$  is the likelihood of the signal vector  $\mathbf{a}_{\ell m}$  given the data  $\mathbf{D}_{\ell m}$ . The prior probability  $\Pr(\mathbf{a}_{\ell m})$  contains our previous knowledge or assumptions about the signal vector before acquiring any data. In the case of the maximum-entropy method the specific feature that distinguishes it from other Bayesian component separation algorithms is that it assumes the prior to be of entropic form,  $\Pr(\mathbf{h}_{\ell m}) \propto \exp[\alpha S(\mathbf{h}_{\ell m}, \mathbf{m})]$ , where the 'hidden' vector  $\mathbf{h}_{\ell m}$  is related to the signal vector by  $\mathbf{a}_{\ell m} = \mathbf{L}_{\ell} \mathbf{h}_{\ell m}$  and  $\mathbf{m}$  is a model vector to which  $\mathbf{h}_{\ell m}$  defaults in the absence of data.  $S(\mathbf{h}_{\ell m}, \mathbf{m})$ , whose form has been derived in Gull & Skilling (1990) and Hobson & Lasenby (1998), is the cross-entropy of  $\mathbf{h}_{\ell m}$  and  $\mathbf{m}$  and  $\alpha$  is a regularisation parameter, which is treated as another optimisation hypothesis parameter.  $\mathbf{L}_{\ell}$  is obtained by a Cholesky decomposition of the isotropic signal

covariance matrix  $\mathbf{C}_{\ell} = \langle \mathbf{a}_{\ell m} \mathbf{a}_{\ell' m'}^{\dagger} \rangle$ . Using such an entropic prior instead of a Gaussian, as is the case when Wiener filtering, ensures a better reconstruction of non-Gaussian components such as the thermal and kinematic SZ effect.

A maximisation of the posterior with respect to  $\mathbf{a}_{\ell m}$  is therefore equivalent to minimising the function

$$\Phi(\mathbf{h}_{\ell m}) = \chi^2(\mathbf{h}_{\ell m}) - \alpha S(\mathbf{h}_{\ell m}, \mathbf{m}), \quad (28)$$

since assuming Gaussian instrumental noise

$$\Pr(\mathbf{d}_{\ell m} | \mathbf{h}_{\ell m}) \propto \exp[-\chi^2(\mathbf{h}_{\ell m})], \quad (29)$$

where  $\chi^2$  is the standard misfit statistic which utilises the isotropic noise covariance matrix  $\mathbf{N}_{\ell} = \langle \boldsymbol{\epsilon}_{\ell m} \boldsymbol{\epsilon}_{\ell' m'}^{\dagger} \rangle$ .

To recover the SZ signal with the HSMEM, prior knowledge about cross-correlation between different components has not been assumed. Nevertheless, prior knowledge about the approximate shape and amplitude of the component power spectra is included in the analysis. This assumption is reasonable since preceding observations and data analysis of Planck observations themselves will provide prior constraints on the component power spectra.

### 4.2 Cluster detection algorithm

To obtain the thermal SZ signal of single clusters the HSMEM recovered thermal SZ map is searched for local maxima above a certain threshold, which can be optimised to maximise the number of detected clusters and to minimise the number of false detections. A cluster is considered to be detected when the true position of its peak signal coincides with a local maximum found in the reconstructed map to within a defined off-set around the peak. In the work presented here an off-set of one map pixel size ( $\approx 2$  arcmin; chosen to be just below the Nyquist sampling for the smallest Planck beam) has been allowed in the case the cluster's core radius angular extent is smaller than the size of a pixel. This applies to the vast majority of galaxy clusters. Otherwise the local maximum (in the following also referred to as SZ peak detection) has to lie within the core radius of the true cluster to be matched. This choice of off-set has been found to be optimal in order to obtain a high matching rate and avoid ambiguities arising from several maxima or clusters being matched to one of the other kind. Only maxima whose amplitude is greater than a fixed multiple of the estimated noise rms of the reconstructed map,  $\sigma_{noise}$ , (minimally  $3 \times \sigma_{noise}$ ) have been taken into account. The rms of the reconstructed map is obtained iteratively by masking maxima and their surroundings which are likely to belong to a cluster detection. Starting with the rms obtained over the whole map we exclude maxima above a threshold, for example  $5 \times \sigma_{noise}$ , and their environment which is assigned to them by flux integration. This process is repeated until the rms has converged.

If a maximum can be matched to several clusters or several maxima can be matched to one cluster then an amplitude and offset comparison is carried out in order to obtain the most likely match. In the case of extended clusters it can happen that due to noise (and background confusion) several maxima belong to the same cluster. Therefore, if maxima fall within each others estimated radius they are assumed to relate to the same extended cluster.

<sup>2</sup> [http://astro.esa.int/Planck/science/performance/perf\\_top.html](http://astro.esa.int/Planck/science/performance/perf_top.html)

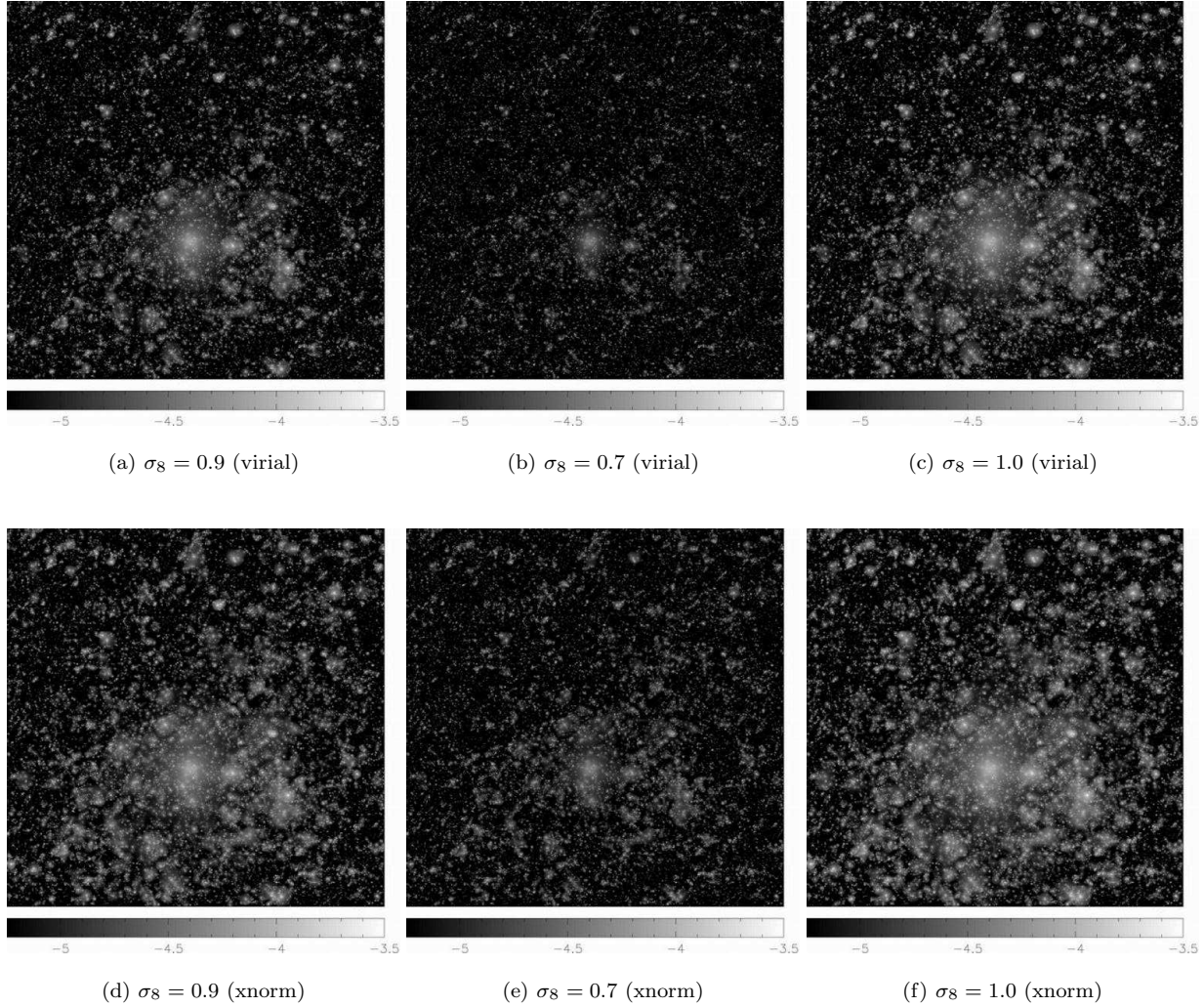


**Figure 2.**  $12.5 \times 12.5 \text{deg}^2$  thermal SZ realizations of the same patch of sky for three different values of  $\sigma_8$  and two different M-T scaling relations (see equation 9 and text) for the  $\Lambda\text{CDM}$  model (see Table 1) used to make simulated *Planck Surveyor* observations. The value of  $\sigma_8$  and the M-T relation used in the particular realization are given below each panel. The maps are shown in units of the frequency independent Compton  $y$  parameter.

The integrated Comptonization parameter  $Y$  and cluster radius  $r_{cl}$  associated with a SZ peak detection are estimated by spherical flux integration. At the radial extent at which the change in the interior integrated flux falls below a certain threshold, i.e. the contribution which is expected to be due to  $3 \times \sigma_{noise}$ , the cluster is cut off. This ensures that the signal-to-noise ratio of cluster detections is at least 3.

Even though recently more sophisticated algorithms have been suggested, such as the pseudo optimal filter (Heranz et al. 2002) and MCMC methods (Hobson & McLachlan 2003), we decided to use the presented algorithm since it is efficient and has the ability to provide robust results (see section 5.2). The advantage of the algorithm presented here is that, besides the assumption of the cluster to be spherical, the flux estimate is independent of the chosen cluster profile. This is not the case for a pseudo optimal matched filter or MCMC application. The assumption that the cluster shape is spherical should be a fair approximation for most clusters,

since X-ray observations show that the clusters' median ellipticity is  $\approx 0.2$  (see Mohr et al. 1995).

We tested the assumptions on which the matching algorithm relies, such as the choice of the acceptance region and the association of multiple SZ peaks to a single extended cluster, and found, even though further optimisation may still be possible, that our choices are reasonable and do not affect the obtained completeness and purity estimates to a great extent. Nevertheless, problems which we found are discussed in the text below (see section 5.2). Furthermore, we note that it is most likely that the final analysis performed on the Planck data will consist of a combination of several methods making optimal use of their different advantages, such as speed, detection efficiency and prior knowledge, at different levels of the analysis to maximise the number of cluster detections and the speed of the analysis.



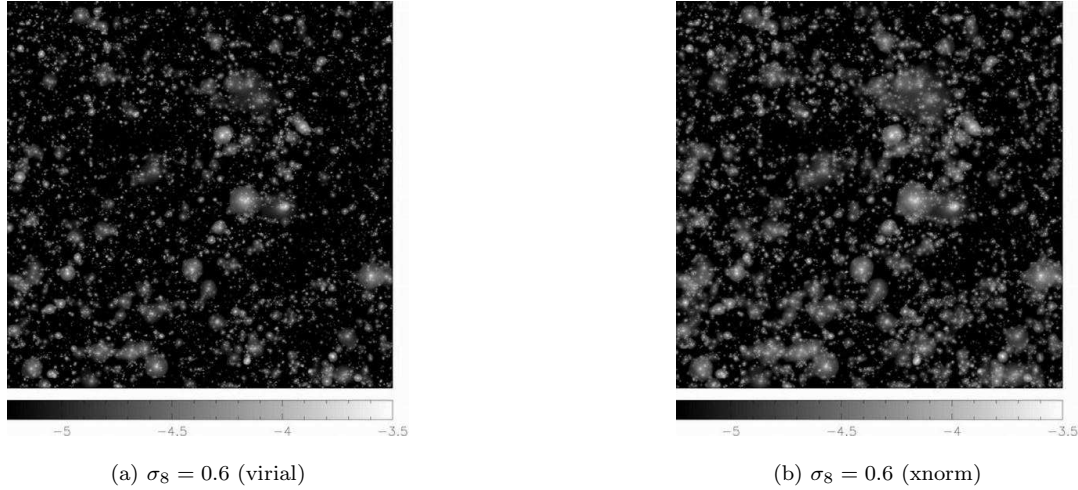


**Figure 3.** The same as Figure 2 for the  $\tau$ CDM model (see Table 1). Here a value of  $\sigma_8 = 0.6$  has been used together with the different M-T relation normalisations to produce the thermal SZ simulations.

## 5 RESULTS AND DISCUSSION

Based on the modelling described above, full-sky maps of the SZ effects are constructed. Patches of the Compton  $y$  maps of the thermal SZ effect for different values of  $\sigma_8$  and different M-T relations are shown in Figures 2 and 3 for the  $\Lambda$ CDM and  $\tau$ CDM cosmology respectively. The models have been chosen to cover a wide range of parameter space. In particular, models which are supported by recent observations, such as the WMAP mission and X-ray cluster and weak lensing measurements, have been included. Moreover, the model choice has been influenced by observational data of the CMB at high angular multipoles ( $1500 < l < 3000$ ). To visualise the differences occurring from changes in  $\sigma_8$  and of the M-T relation, the same sky patch is shown for the  $\Lambda$ CDM and  $\tau$ CDM models respectively. Due to different structure formation histories the surface density of extended low redshift foreground clusters is larger in the  $\tau$ CDM model, whereas the  $\Lambda$ CDM models possess more high redshift background clusters.

In Figures 4 and 5 the primordial CMB normalised to WMAP measurements at low multipoles and thermal SZ power spectra (in the following referred to as SZ power spectra) are plotted at 300 GHz. The included points with error bars are observational results from ACBAR (Kuo et al. 2002) and CBI (Mason et al. 2001). The measurements have been converted from the particular instrument observing frequency to 300 GHz after subtraction of the primordial CMB contribution by assuming that the remaining measured excess is entirely due to the SZ effect and by using the spectral SZ frequency dependence (see equation 2). The fraction contributed by the primordial CMB has been estimated from an extrapolation of the WMAP results best-fitting primordial CMB power spectrum to higher multipoles, which has been normalised to the height of the first acoustic peak. Further, it has been assumed that the primordial CMB estimate is free of error. Note that, at  $1\sigma$  level, no excess is required to explain the ACBAR measurements. However, under the made assumptions the measured values of ACBAR and CBI are consistent with each other, the SZ interpreta-

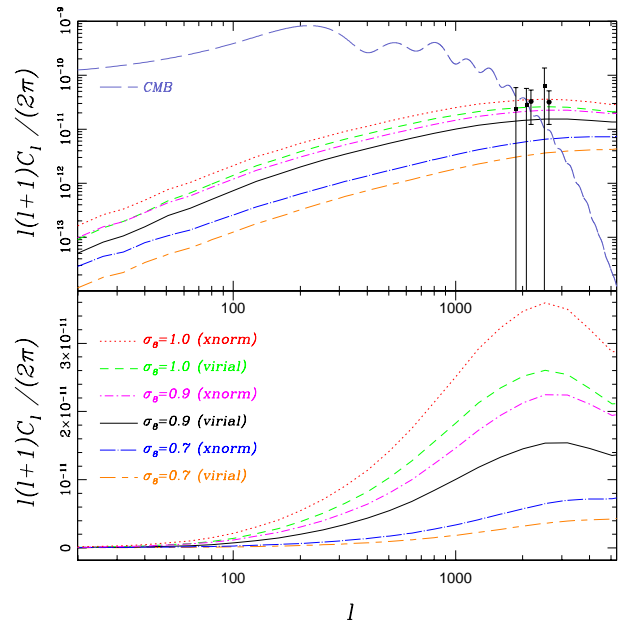


**Figure 4.** The power spectra of the primordial CMB and the SZ effect for different values of  $\sigma_8$  and M-T relations (see panel and text) at 300 GHz for the  $\Lambda$ CDM simulations. While the upper panel shows a log-log plot, in the lower panel the SZ power spectra amplitudes are plotted on a linear scale in order to emphasise the different slopes and multipoles at which the SZ power spectra peak given different values of  $\sigma_8$ . The upper panel includes the CMB excess power spectrum amplitudes as measured by the instruments, CBI (circles) and ACBAR (squares). The measurements have been converted from their values at the particular instrument observing frequency to 300 GHz after subtraction of the primordial CMB contribution (see text for details) by assuming that they are entirely due to the SZ effect and by then using the spectral SZ frequency dependence (see equation 2).

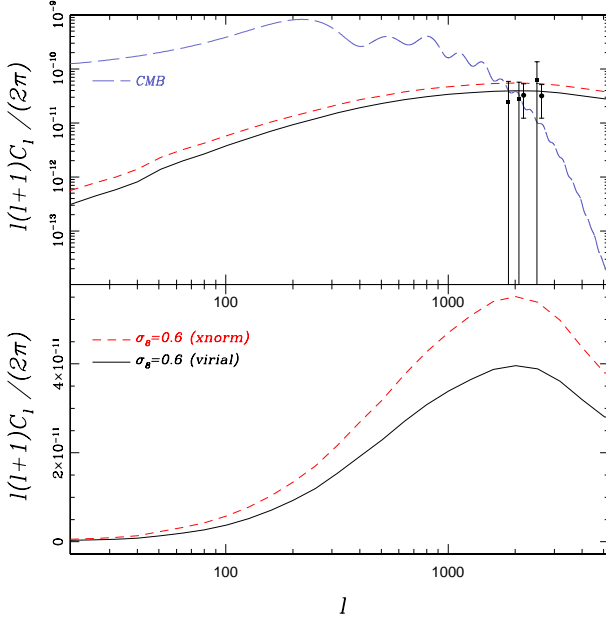


**Figure 5.** The same as Figure 4 for the  $\tau$ CDM simulations.

tion and the primordial CMB contribution estimated on the basis of the WMAP measurements. The consistency of the CBI and ACBAR excesses has also been found by Goldstein et al. (2003) by simultaneously fitting primordial CMB and SZ power spectra to the observations without using WMAP constraints. While the high- $\sigma_8$   $\Lambda$ CDM model SZ power spectra fit the observed excess measurements well, the lower  $\sigma_8$   $\Lambda$ CDM models tend to lie below the excess measured by CBI and ACBAR. This finding is consistent with Bond et al. (2002) who obtained  $\sigma_8 = 1.0$  using SZ power spectra from hydrodynamical simulations to fit the CBI excess for  $\Lambda$ CDM cosmologies. The  $\tau$ CDM  $\sigma_8 = 0.6$  SZ power spectra slightly overpredict the SZ power compared to the observed excess (but they are excluded by less than  $1\sigma$ ). Nevertheless, for the presented work it is important to include a wide range of models in order to study model dependent selection effects of the employed cluster detection algorithm.

### 5.1 The SZ power spectrum relation to $\sigma_8$

Since the value of  $\sigma_8$  has a significant effect on the abundance of galaxy clusters and thus on the measured power of SZ anisotropies, in the following the dependence of the thermal SZ power spectrum amplitude on  $\sigma_8$  is investigated on the basis of the performed simulations. Predictions by various authors (Komatsu & Kitayama 1999; Seljak et al. 2001; Zhang & Pen 2001; Komatsu & Seljak 2002; Sadeh & Rephaeli 2004) expect  $C_l \propto (\Omega_b h)^2 \sigma_8^{4-7}$ . Based on such predictions Bond et al. (2002) estimated  $\sigma_8 \approx 1.0$  from the excess power at high  $l$  values measured by the CBI experiment using hydrodynamical simulations of the SZ effect.

Most of the previous work on the SZ power spectrum dependence on  $\sigma_8$  utilised either a standard Press-Schechter mass function (Press & Schechter 1976) or hydrodynamical simulations of small sky patches to obtain SZ power spectra. Komatsu & Seljak (2002) used the Jenkins mass function

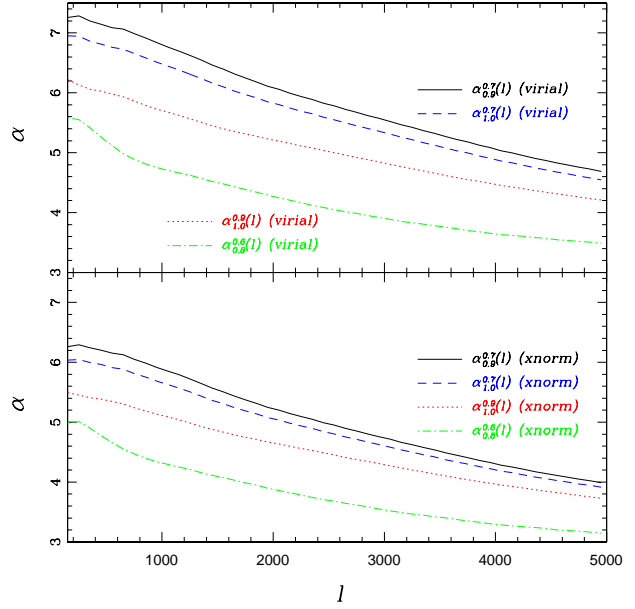


**Figure 6.** The dependence of the power law index  $\alpha$  on the multipoles  $l$  for the virial (upper panel) and the M-T relation obtained from X-ray observations (lower panel) for our modelling of the SZ sky.

(Jenkins et al. 2001), on which also the mass function of Evrard et al. (2002) is built, and a cluster pressure profile fitted to hydrodynamical simulations to evaluate the dependence of the SZ power spectrum coefficients on cosmological parameters, especially  $\sigma_8$ , for the Poissonian contribution at small angular scales. Being based on the HV simulations our simulations ensure a realistic modelling of the clustering contribution of galaxy clusters to the SZ power spectrum.

Moreover, the mass cut can affect the SZ power spectrum estimation. For the simulated  $\Lambda$  and  $\tau$ CDM models we performed a mass cut at  $M_{cl} \approx 3 \times 10^{13} h^{-1} M_\odot$ . Komatsu & Seljak (2002) find that a mass cut as low as  $5 \times 10^{12} h^{-1} M_\odot$  is sufficient to obtain the SZ power spectrum independently of mass boundaries for scales up to  $l \approx 10^4$ . For such low ‘cluster’ masses the applicability of the scaling relations as derived in section 3 is questionable, since observations indicate a steepening of the M-T relation at mass scales of the order of  $1 \times 10^{13} h^{-1} M_\odot$  (Finoguenov et al. 2001; Borgani et al. 2002). On the angular scales of interest the performed mass cut suffices to ensure independence of the SZ power spectrum. This has been tested by a comparison of the SZ power spectra obtained by performing different mass cuts and on this basis the performed mass cut has been found to be sufficient. For example, if we raise the mass cut from  $3 \times 10^{13} h^{-1} M_\odot$  to  $5 \times 10^{13} h^{-1} M_\odot$ , a decrease of the SZ power spectrum amplitude at  $l = 5000$  of approximately 10 per cent is found. Anyway, since most of the clusters of the Planck survey will be unresolved (see section 5.3), Planck’s ability to study substructures and cluster physics will be (very) limited. Therefore, small mass clusters are mainly included to provide a realistic SZ background noise.

Nevertheless, we present in the following an estimation based on our cluster modelling of the dependence of the thermal SZ power spectrum amplitude on  $\sigma_8$  over a wide

range of angular scales  $l$ . Expressing the relation between the SZ power spectrum amplitude and  $\sigma_8$  by

$$C_l \propto \sigma_8^\alpha, \quad (30)$$

$\alpha$  is obtained for two particular realisations of different  $\sigma_8$  by

$$\alpha(l) = \frac{\log \left( C_l(\sigma_8^{(1)}) / C_l(\sigma_8^{(2)}) \right)}{\log \left( \sigma_8^{(1)} / \sigma_8^{(2)} \right)}. \quad (31)$$

In Figure 6 the dependence of  $\alpha$  on  $l$  is plotted for different combinations of  $\sigma_8^{(1)}$  and  $\sigma_8^{(2)}$  for the used M-T relations (see section 3.2.1).

Given our modelling of the SZ effect,  $\alpha(l)$  is found to exhibit a significant negative slope. While for the  $\Lambda$ CDM models at low multipoles  $\alpha$  adopts values of approximately 6 to 7, on small angular scales ( $l \geq 3000$ ) it has fallen to values of at least a unit less. This behaviour can explain the wide range of values found in the literature for the power-law index  $\alpha$ . Sadeh & Rephaeli (2004) obtained from analytical estimates of the SZ power spectrum using the cluster gas profile of equation (18)  $C_l \propto \sigma_8^4$  at high  $l$ s, while previous studies at lower  $l$ s estimated  $C_l \propto \sigma_8^{6-7}$  (see e.g. Komatsu & Kitayama 1999). Thus it has to be taken into account for which multipole range  $\alpha$  is evaluated. Partially, this behaviour is due to the clustering contribution which is most significant on large angular scales and has been shown to possess a stronger scaling with  $\sigma_8$  (Komatsu & Kitayama 1999).

In the case of hydrodynamical simulations the contribution due to substructure, which is expected to increase the SZ power on small angular scales, possibly modifies the behaviour of the power-law index  $\alpha$  at high multipoles. As some hydrodynamical simulations have been found to disagree with each other, it is at present impossible to make robust predictions. For example, the mesh-based GADGET code of Springel, White & Hernquist (2001) seems to predict more small-scale power than the simulations of da Silva et al. (2001) using HYDRA, a SPH code. Since the SPH simulations of Bond et al. (2002) agree in shape with Springel, White & Hernquist (2001), the disagreement is unlikely to be dependent on the differences of the applied methods. The different shape of the high- $l$  SZ power spectra of various hydrodynamical simulations could be due to a resolution effect. The higher the resolution of the simulation the more substructure is revealed which increases the amplitude of the power spectrum at high multipoles and also flattens its peak. da Silva et al. (2004) state that they have not yet attempted a resolution study of their code. Anyway, since hydrodynamical simulations are computationally expensive it is currently unfeasible to simulate volumes of the size needed for realistic full-sky simulations of Planck observations.

Furthermore, in the case of the M-T relation derived from X-ray measurements the power-law index systematically takes on smaller values than for the virial M-T relation. This is due to the difference of the cluster Compton  $y$  profile induced by the change in temperature corresponding to a fixed cluster mass. Since the cluster radius and central electron gas density scale only with cluster mass and redshift (see section 3), the  $y$  profile of the cluster is altered by the increase of  $T_e$ . In our modelling the outskirts of the

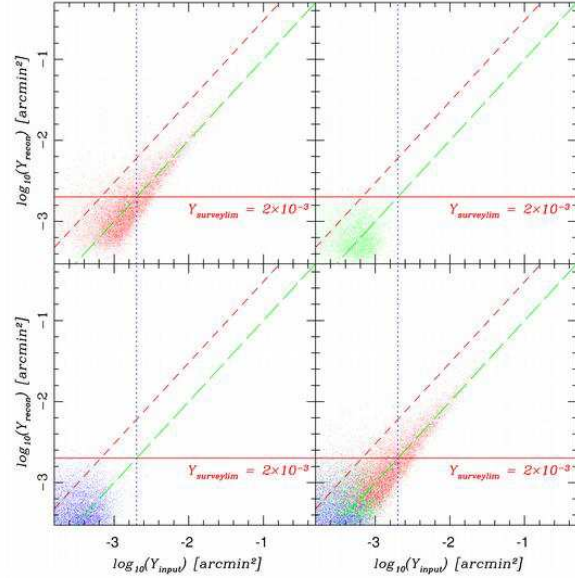


**Figure 7.** Scatter plot of the reconstructed versus the actual cluster Comptonization parameter  $Y$  for clusters which have been matched to a SZ peak detection by the described algorithm (see section 4.2) for the fiducial  $\Lambda$ CDM model (see Table 1). Based on the cluster detection algorithm the upper left, the upper right and the lower left panel show the scatter of the reconstructed cluster fluxes for clusters with a peak detection of 5, 4 and 3 times  $\sigma_{\text{noise}}$ . The long dashed green line gives the optimal reconstruction. The horizontal red line represents a conservative survey  $Y$  limit estimate. It is chosen to lie well above the ‘confusion plateau’ level. The dotted vertical blue line shows the same flux limit for  $Y_{\text{input}}$  ( $Y_{\text{input}} \approx 2 \times 10^{-3} \text{ arcmin}^2$ ). Due to cluster-cluster confusion even low flux clusters of  $Y \approx 1 \times 10^{-4} \text{ arcmin}^2$  can have an associated  $Y_{\text{recon}}$  of several  $1 \times 10^{-4} \text{ arcmin}^2$ . The dashed red line gives a tolerant upper limit for when a cluster-SZ peak match is taken to be correct. This has been estimated from the skewness of the scatter around the optimal cluster flux reconstruction and is chosen to be  $3 \times Y_{\text{input}}$  (see text for detailed explanation). The lower right panel shows all detections.

cluster are more affected by this modification of the profile than its core and therefore the effect is more significant at low multipoles.

As Figure 6 shows the power-law index  $\alpha$  takes on a lower value in the case of the  $\tau$ CDM models. This agrees with the analytic expectations derived in Komatsu & Seljak (2002). Moreover, the peak of the SZ power spectrum is shifted towards smaller angular scales for smaller values of  $\sigma_8$  (see lower panels of Figures 4 and 5) due to the rescaling of cluster masses (see equation 24) and thus resizing of the clusters.

## 5.2 The reconstructed SZ flux number count

First we consider the concordance cosmological model, the  $\Lambda$ CDM model, which is supported by the WMAP measurements (Bennett et al. 2003), together with the virial M-T relation as our fiducial model. In particular the adopted cosmological parameters are  $\Omega_m = 0.3$ ,  $\Omega_\Lambda = 0.7$ ,  $H_0 = 100 h \text{ km s}^{-1} \text{ Mpc}^{-1}$  with  $h = 0.7$ ,  $\Omega_b = 0.04$ ,  $n = 1$  and  $\sigma_8 = 0.9$  since these model parameters yield a reasonable

<i>Model</i>	<i><math>\tau</math>CDM</i>	
	0.6 (virial)	0.6 (xnorm)
<i><math>\sigma_8</math> and <math>M</math>-<math>T</math> relation</i>		
$n_{cl}(Y_{input} \geq 5 \times 10^{-3})$	3043	4620
$n_{cl}(Y_{recon} \geq 5 \times 10^{-3})$	3070	4800
$n_{cl}(Y_{input} \geq 4 \times 10^{-3})$	4134	6243
$n_{cl}(Y_{recon} \geq 4 \times 10^{-3})$	4194	6602
$n_{cl}(Y_{input} \geq 3 \times 10^{-3})$	6030	9264
$n_{cl}(Y_{recon} \geq 3 \times 10^{-3})$	6200	9803
$n_{cl}(Y_{input} \geq 2 \times 10^{-3})$	10441	16051
$n_{cl}(Y_{recon} \geq 2 \times 10^{-3})$	10523	16729
$n_{cl}(Y_{input} \geq 1 \times 10^{-3})$	25410	39689
$n_{cl}(Y_{recon} \geq 1 \times 10^{-3})$	24160	36155

**Table 4.** The same as Table 3 for the  $\tau$ CDM model.

fit to the current strong cosmological constraints and thus provide a robust basis for making realistic predictions. Furthermore, these parameters agree with the  $\Lambda$ CDM HV N-body simulations used to obtain the thermal and kinematic SZ maps.

Figure 7 shows the scatter of the reconstructed SZ cluster integrated Comptonization parameters versus their real ones. The reconstructed  $Y$ s have been obtained by applying the algorithm as described in section 4.2. Only clusters whose real Comptonization parameter  $Y$  lies above  $1 \times 10^{-4} \text{ arcmin}^2$  have been matched to detected SZ peaks. This assumed lower sensitivity limit of  $Y$  has been suggested by analytical considerations (see e.g. Bartelmann 2001). In Figure 7 the scatter of  $Y$  of detected clusters is shown for different peak detection thresholds ( $5$ ,  $4$  and  $3 \times \sigma_{noise}$ ). Even though the majority of detections with a peak above  $4$  or  $3 \times \sigma_{noise}$  scatters symmetrically around the line of optimal detection and therefore can be believed to be matched up correctly, there is also a significant fraction which is scattered upwards to larger fluxes. These detections are either false matches or - which is more often the case - up-scattered due to cluster-cluster confusion. Thus for lower real cluster fluxes the reconstructed integrated Comptonization parameters level off. The shown survey limit estimate ( $Y_{surveylim} = 2 \times 10^{-3} \text{ arcmin}^2$ ) is chosen to lie well above this flux ‘plateau’ to ensure that the reconstructed flux distribution represents closely the real one. As Figure 7 illustrates, the contribution of  $3$ - and  $4$ - $\sigma_{noise}$  peak detections above the sensitivity estimate for Planck is small.

The reconstructed fluxes of some clusters are upscattered due to cluster-cluster confusion and even for the  $5 - \sigma_{noise}$  detections the scatter around the optimal reconstruction is slightly skewed. Hence, there happen to be some outliers whose reconstructed  $Y$  is several times their  $Y_{input}$ . One way to deal with this is the introduction of a liberal upper  $Y$ -limit that ensures that these questionable cluster reconstructions can be excluded from the sample. Thus by enforcement of this limit clusters with a reconstructed  $Y_{recon}$  above  $3 \times Y_{input}$  are regarded as false detections. On first sight this choice seems to be quite high, but one has to keep in mind that clusters confusing each other often have comparable masses and are situated next to each other in redshift space. In the following estimates

of detection purity and completeness of the presented cluster detection method are given with and without taking account of this upper limit. Furthermore, these characteristics of the algorithm are shown for all cluster detections with associated peaks above  $3 \times \sigma_{noise}$  as well as only for the  $5 - \sigma_{noise}$  peak detections. Since the reconstructed integrated Comptonization parameters of high-flux clusters scatter almost symmetrically around the line of optimal flux reconstruction, this indicates that the estimate of the total cluster flux obtained by our algorithm for clusters above  $Y_{surveylim} = 2 \times 10^{-3} \text{ arcmin}^2$  is fairly unbiased. The leveling off of the reconstructed  $Y$ s at lower fluxes is mainly due to clusters being confused with each other.

The completeness and purity obtained by the applied algorithm are plotted in Figure 8 for the full-sky simulation and for a Galactic cut of Galactic latitude  $|b| \leq 20^\circ$ . The Galactic cut has been performed in order to evaluate the influence of Galactic residuals in the thermal SZ reconstruction on the quality of the obtained cluster number count. For the full-sky cluster number count, the cluster survey is more than 83 per cent complete and the purity exceeds 88 per cent above the estimated survey limit,  $Y_{surveylim} = 2 \times 10^{-3} \text{ arcmin}^2$ , for all clusters without enforcement of an upper matching limit. While the completeness is unaffected by the introduction of the proposed upper  $Y$ -limit, the purity estimate is reduced by approximately 5 per cent. This is the case when all detected clusters are considered as well as for only considering  $5 - \sigma_{noise}$  peak detections. In any case neither the purity nor the completeness fall below 80 per cent for  $Y_{surveylim} = 2 \times 10^{-3} \text{ arcmin}^2$  for a cluster survey performed over the full sky. In the case of the Galactic cut, the completeness is increased by a few per cent, whereas the purity is barely improved for clusters with  $Y$  above  $2 \times 10^{-3} \text{ arcmin}^2$ . Thus the Galaxy does not introduce significantly false detections into the recovered cluster sample. Some clusters are missed due to Galactic contamination. However, the improvement of the completeness is mostly cancelled by the reduction in the number of detected clusters which leads to an increase in the Poissonian sampling error of about the same percentage at  $Y_{surveylim} = 2 \times 10^{-3} \text{ arcmin}^2$ .

Note that the resulting completeness and purity also depend on the reliability of the cluster-SZ peak matching. Since the number of clusters and SZ peaks which have to be matched is large, the matching has to be automated. Even though an optimisation has been performed, it occasionally happens that the algorithm fails to match clusters and SZ peak detections correctly. The number of false detections and undetected clusters are both increased if a SZ peak which actually corresponds to a cluster is not matched up. This occurs, for example, in the case in which two clusters are confused with each other by beam-convolution and the SZ peak corresponding to both lies outside the matching acceptance region. Therefore, the quoted values have to be regarded as conservative lower limits of the cluster finding algorithm. This is supported by the comparison of the number of detected SZ peaks whose flux estimation exceeds the sensitivity limit and the number of clusters above  $Y_{surveylim} = 2 \times 10^{-3} \text{ arcmin}^2$  which are contained in the map (see Tables 3 and 4).

Figure 9 shows the differential number redshift distribution of clusters with and without a performed Galactic cut



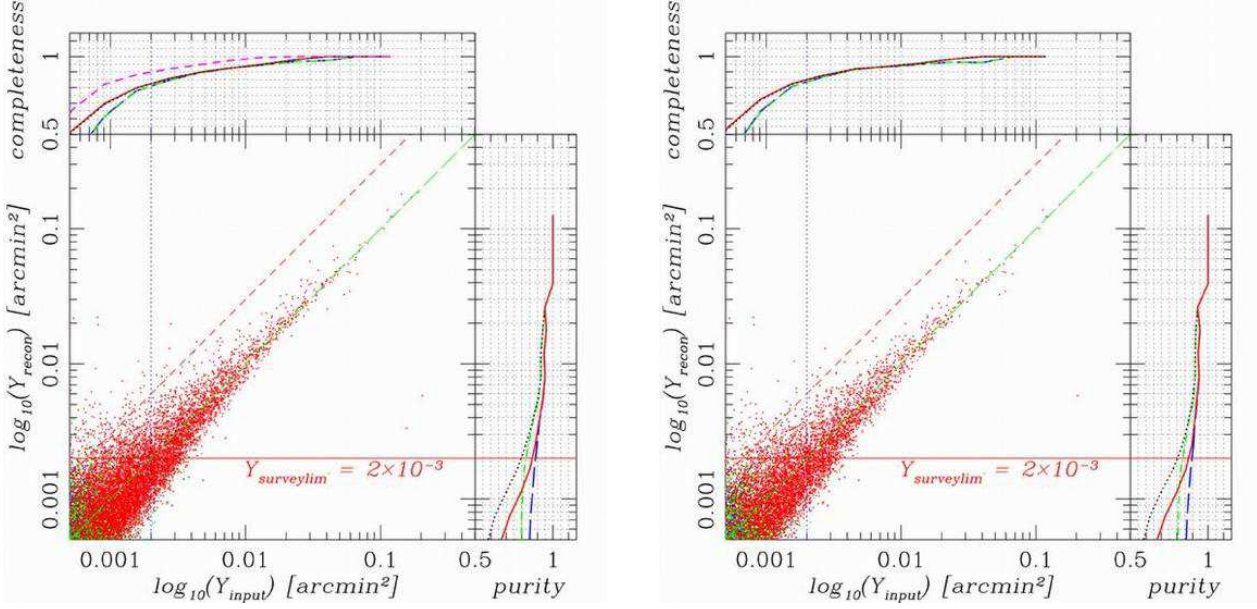


**Figure 8.** In the left panel the same scatter as in Figure 7 is shown (for comparison), while a Galactic cut of  $\pm 20^\circ$  Galactic latitude has been performed to obtain the scatter in the right panel. In this Figure the completeness and purity of the reconstructed cluster sample are shown. In the purity and completeness plots the red solid line represents the case in which all detections with a peak amplitude above  $3 \times \sigma_{noise}$  are taken into account, the blue long-dashed the case which utilises only detections whose peak amplitude is  $\geq 5 \times \sigma_{noise}$ . The black dotted line and the green short-dashed line show both cases when the matches which scatter above the red dashed diagonal line are not approved as detections. In the left panel the magenta short-dashed line gives the completeness of the survey when multiple clusters are allowed to be matched to a single detection peak.

Model	$\Lambda$ CDM					
$\sigma_8$ and M-T relation	0.7 (virial)	0.7 (xnorm)	0.9 (virial)	0.9 (xnorm)	1.0 (virial)	1.0 (xnorm)
$n_{cl}(Y_{input} \geq 5 \times 10^{-3})$	219	405	959/642	1462	1575	2299
$n_{cl}(Y_{recon} \geq 5 \times 10^{-3})$	260	497	957/662	1493	1528	2266
$n_{cl}(Y_{input} \geq 4 \times 10^{-3})$	307	573	1348/903	2053	2206	3206
$n_{cl}(Y_{recon} \geq 4 \times 10^{-3})$	379	699	1325/905	2062	2093	3186
$n_{cl}(Y_{input} \geq 3 \times 10^{-3})$	480	899	2083/1403	3207	3350	4801
$n_{cl}(Y_{recon} \geq 3 \times 10^{-3})$	625	1128	2000/1371	3193	3180	4920
$n_{cl}(Y_{input} \geq 2 \times 10^{-3})$	930	1741	3781/2561	5770	5941	8701
$n_{cl}(Y_{recon} \geq 2 \times 10^{-3})$	1478	2360	3659/2532	5998	5784	9035
$n_{cl}(Y_{input} \geq 1 \times 10^{-3})$	2791	5263	10228/6735	16114	15773	23826
$n_{cl}(Y_{recon} \geq 1 \times 10^{-3})$	5506	7764	10744/7405	16626	15736	23358

**Table 3.** Cluster number counts above certain limits of the Comptonization parameter  $Y$  for the  $\Lambda$ CDM models with different  $\sigma_8$  and for the two utilised M-T relation normalisations. In each case the expected input and recovered number of clusters above the assumed  $Y$  limit (in  $\text{arcmin}^2$ ) is given. In the virial  $\sigma_8 = 0.9$  case the stated numbers are for a full-sky survey as well as for one with a Galactic cut of  $\pm 20^\circ$  Galactic latitude (utilising 2/3 of the sky).

as compared to the expected one for  $Y \geq 2 \times 10^{-3} \text{ arcmin}^2$ . The largest difference between the expected distribution and the recovered ones occurs at low redshifts. This is mainly due to cluster-cluster confusion by beam-convolution. Due to line-of-sight projection, an extended foreground cluster is more likely to overlap with background clusters. Part of this observed effect, however, is caused by the reconstruction noise, since extended foreground clusters have smaller signal-to-noise peak detections than high-redshift clusters

which appear more compact when projected along the line-of-sight. At higher redshifts the differential reconstructed number counts sometimes exceed those expected. This is due to clusters whose real fluxes are just below the survey threshold and being upscattered due to confusion of their SZ signal by projected overlapping clusters. The Galactic cut distribution yields slightly better results than the full-sky one.

In Figure 10 results of the application of the algorithm

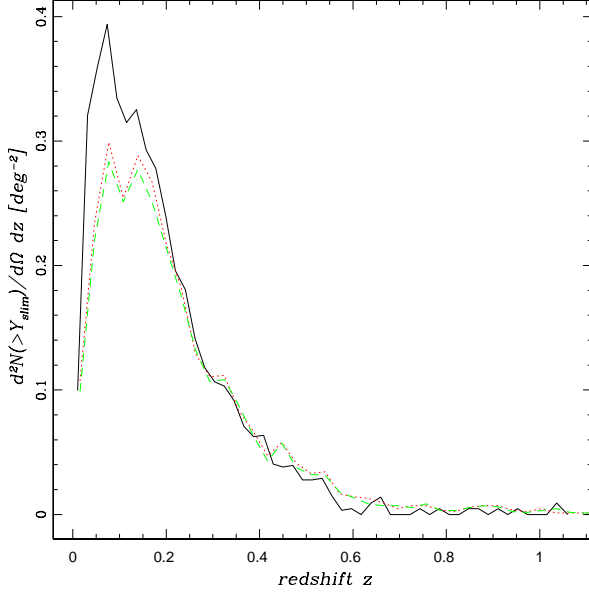


**Figure 9.** The differential cluster number redshift distribution per square degree for the HV cluster catalogue (black solid line), for the full-sky recovered galaxy cluster survey (green dashed line) and when performing a Galactic cut of  $\pm 20^\circ$  Galactic latitude (red dotted line) for an assumed survey sensitivity limit of  $Y_{\text{surveylim}} = 2 \times 10^{-3} \text{ arcmin}^2$ .

to models with cosmological parameters which differ from the concordance model are shown. This has been done to test the algorithm which has been optimised for the fiducial  $\Lambda\text{CDM}$  cosmology. The models are chosen to incorporate a wide range of  $\sigma_8$  which is still allowed by observations to ensure that in any case the method delivers reliable results. The WMAP measurements on their own do not put strong constraints on  $\sigma_8$ . Hence,  $\sigma_8 = 0.7$  has been taken as the lower limit of the allowed range as this value is currently supported by X-ray cluster survey analyses (Allen et al. 2003). On the other hand weak lensing observations tend to favour higher values (see e.g. Hoekstra et al. 2002; Bacon et al. 2003). Thus  $\sigma_8 = 1.0$  may be considered as an upper limit of the allowed range. Besides the favoured  $\Lambda\text{CDM}$  model we include a flat model dominated by non-relativistic matter without a cosmological constant ( $\tau\text{CDM}$  model) in our investigations.

We find, apart from the low- $\sigma_8$   $\Lambda\text{CDM}$  model, the estimated completeness as well as purity obtained for the additional models are of equivalent or even improved quality in comparison to estimates for the concordance model and the virial M-T relation.

In the case of the low- $\sigma_8$   $\Lambda\text{CDM}$  models noise introduced by the HSMEM itself and residual noise of other components become more significant due to the lower SZ signal amplitude. The completeness and purity for all cluster counts with  $Y$  above the survey limit are reduced to 56 and 68 per cent respectively (without enforcement of an upper matching limit). Thus, the applied algorithm does not quite suffice anymore to provide a reconstruction quality from which tight constraints on cosmological parameters,

$\sigma_8$  and  $\Omega_m$ , can be derived or which can establish a robust basis for successful follow-up observations.

Moreover, for models with a larger variance of matter fluctuations on scales of  $8 h^{-1} \text{ Mpc}$ , the cluster confusion is more significant. Due to the mass rescaling obtained by employing equation (24) a cluster gets associated with a larger mass and therefore has a larger extent. This results in a more significant cluster overlap when projecting clusters SZ signal onto the two-dimensional full-sky map. As a result the completeness slightly decreases due to increasing cluster-cluster confusion. On the other hand the purity is slightly increased due to the more dominant SZ signal. A similar effect is generally found when the cluster temperatures are increased by a change of the M-T scaling relation normalisation. Then due to beam-convolution neighbouring clusters affect each other more strongly. Even though it can be argued that in any case of cluster-cluster confusion a confirmation procedure would be able to match the contributing clusters and even disentangle their contributions, these more optimistic considerations have not entered the presented results.

Tables 3 and 4 give the detected cluster numbers above a declining threshold for each simulation. For comparison, the number of clusters whose flux exceeds the particular threshold and has been obtained directly from the cluster catalogues is also given. For  $Y_{\text{surveylim}} = 2 \times 10^{-3} \text{ arcmin}^2$  we expect Planck to detect several 1000 clusters. If  $Y_{\text{surveylim}}$  can be lowered to  $1 \times 10^{-3} \text{ arcmin}^2$ , Planck will find a total number of clusters of the order  $10^4$ . Since the recovered and input cluster number show good agreement even for  $Y_{\text{lim}} = 1 \times 10^{-3} \text{ arcmin}^2$ , it is likely that, when the matching of SZ peak detections with clusters is even more optimised, a flux limit of  $1 \times 10^{-3} \text{ arcmin}^2$  may be reached.

So far we have taken into account the quality of the cluster flux recovery to estimate a sensitivity limit for a Planck cluster survey. Previous work often considered a cluster to be detected when it could be successfully matched with a peak in the reconstructed SZ map and allowed even several clusters to be matched with a single SZ peak. It can be argued that follow-up observations at higher resolution or at other wavelengths are able to disentangle the contributions of several clusters to an extended SZ feature and to confirm Planck cluster detections. Such follow-up observations can be performed, for example, by ground-based SZ telescopes, such as the interferometers AMI (Kneissl et al. 2001), Amiba (Lo et al. 2000) and SZA (Mohr et al. 2002) in the northern hemisphere and the upcoming instruments in the south, such as SPT<sup>3</sup> and ACT<sup>4</sup>. If we assume that the contributions of individual clusters can be separated, the completeness is significantly increased (see Figure 7). The obtained cluster sample is 83 per cent complete at  $Y_{\text{lim}} = 1 \times 10^{-3} \text{ arcmin}^2$  and still has a purity of 78 per cent.

For the fiducial  $\Lambda\text{CDM}$  model, Figure 11 compares the effect of these assumptions on the cluster sample obtained for the two considered sensitivity limits by the differential redshift number distributions. It is found that due to cluster-cluster confusion, especially at higher redshifts ( $z \geq 0.3$ ), at which the angular separation of clusters situated next to each other in redshift space is reduced, the recovered dis-

<sup>3</sup> <http://astro.uchicago.edu/spt>

<sup>4</sup> <http://www.hep.upenn.edu/~angelica/act/act.html>

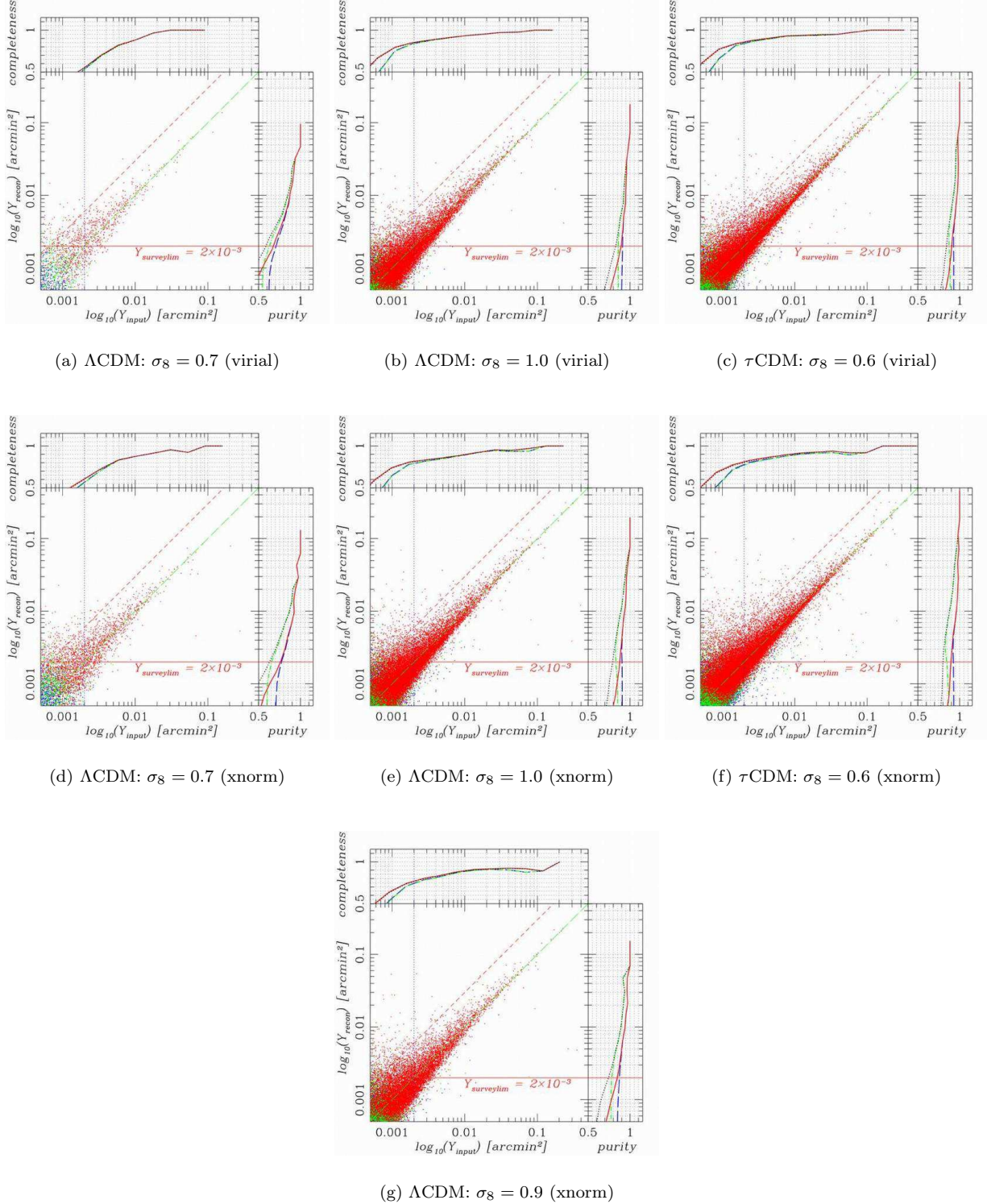


**Figure 10.** The scatter, completeness and purity for all performed cosmological SZ realisations apart from the fiducial  $\Lambda$ CDM one are shown.

tributions using the recovered cluster fluxes exceed the expected cluster numbers significantly for both survey limits. This is caused by an increased likelihood of clusters with fluxes below the particular limit to be included in the sample, since all clusters contributing to the connected peaked

SZ feature are taken into account. On the basis of Planck observations analysed with the presented cluster detection method, it is not possible to separate clusters contributing to a single SZ peak detection. Thus, follow-up observations are unavoidable in order to disentangle clusters and remove



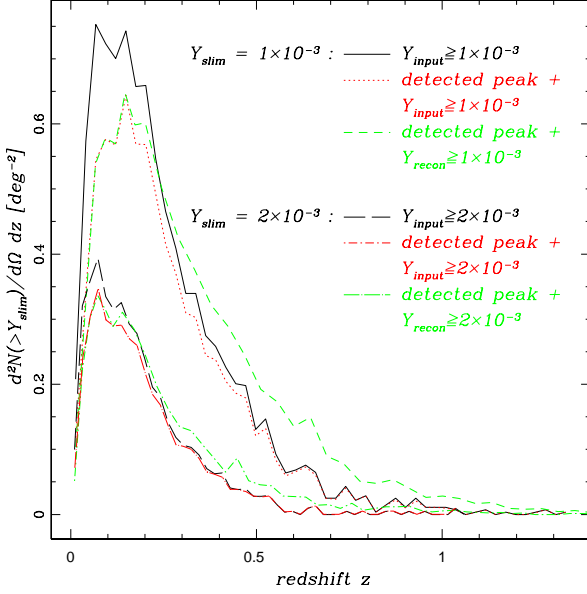


**Figure 11.** The differential cluster number redshift distribution per square degree for the HV input cluster catalogue and for the full-sky galaxy cluster detections under the assumption that a cluster is detected when its matching region includes a reconstructed SZ peak. Thus, multiple clusters can be matched to a single peak. In the case of the peak-detected clusters above a given flux survey limit the distributions are shown for the true cluster flux as well as for the flux associated with the peak matched to the cluster (different distributions are indicated by different colour and line-styles). The plot shows the distributions for assumed survey sensitivity limits of  $2 \times 10^{-3} \text{ arcmin}^2$  and  $1 \times 10^{-3} \text{ arcmin}^2$ .

low-flux clusters contributing to a SZ peak detection above the flux limit from the sample. Then it is feasible to reach the distributions which are given for the cluster peak detections assuming knowledge of the true cluster fluxes (see Figure 11). Further, Figure 11 shows that the recovered distributions (using cluster input as well as recovered fluxes) of the higher survey flux limit ( $Y = 2 \times 10^{-3} \text{ arcmin}^2$ ) resemble the true input distribution more closely than it is the case for the lower flux limit,  $Y_{lim} = 1 \times 10^{-3} \text{ arcmin}^2$ . In the following the more conservative estimate of the sensitivity limit,  $Y_{surveylim} = 2 \times 10^{-3} \text{ arcmin}^2$ , is assumed and only single cluster-peak matches are allowed.

Based on the reconstructed number counts, the purity and completeness estimate, we can examine how likely models exclude each other given the count of a certain model and comparing it to the expected count of the ones that yield similar cluster numbers above the conservative survey limit. This is first done by assuming that our estimates of the percentage of impure and missing clusters are standard deviations of a Gaussian distribution centred on the reconstructed and expected cluster number respectively. Furthermore, we account for the cosmic variance in the number of clusters. Assuming a M-T relation, we find that given the recovered count of a particular model, each of the other models considered here can be excluded by at least  $1.7\sigma$ . This minimal exclusion is obtained in the case of the reconstructed  $\sigma_8 = 0.9$   $\Lambda$ CDM count when compared with the expected count of

the  $\sigma_8 = 1.0$   $\Lambda$ CDM model. However, the  $\sigma_8 = 0.6$   $\tau$ CDM cluster count excludes the  $\sigma_8 = 1.0$   $\Lambda$ CDM model by  $2.6\sigma$ . When we take our estimates of impurity and incompleteness to be absolute values, which have an error themselves, then the probability of exclusion of the respective models with similar expected number counts exceed  $5\sigma$  in all cases. Since these estimates have been obtained by a large number of single cluster detections and we can regard them as the probability that a cluster above the survey limit is detected or a real detection respectively, this assumption should be valid and we can assume a Poissonian sampling error in the completeness and purity. Nevertheless, we first considered the more conservative case of the estimated incompleteness and impurity to be the first moments of a Gaussian distribution of the expected and recovered number count.

As expected the cluster number exceeding a given flux limit is increased for the M-T scaling relation normalised by X-ray observations (xnorm). An uncertainty in the normalisation of the M-T relation introduces extra degeneracies besides the ones present between cosmological parameters. For example, the cluster number yield of the  $\Lambda$ CDM  $\sigma_8 = 0.9$  model employing the xnorm M-T scaling relation is comparable to the one obtained for the  $\Lambda$ CDM  $\sigma_8 = 1.0$  cosmology using the virial M-T relation.

### 5.3 Cluster size distribution and cluster resolution

To study galaxy cluster physics resolution is important. For the Planck satellite, the large beam sizes mean that most clusters will be unresolved. Nevertheless, a minor fraction of the cluster sample, nearby massive clusters, will be resolved. Besides giving an estimate of the expected percentage of resolved clusters contained in the sample above the survey limit estimate ( $Y_{surveylim} = 2 \times 10^{-3} \text{ arcmin}^2$ ), we further investigate how well cluster radii are recovered by the applied cluster finding algorithm.

In Figure 12 we plot the distribution of the cluster angular sizes for a plurality of cluster size definitions. First of all the distribution of the virial radii obtained from the scaling relation (21) is shown. Furthermore, the radius distribution of the beam-convolved cluster extent at which the cluster SZ signal has dropped to half of its peak amplitude is given. This can be compared with the FWHM of the beam estimate of  $9.7 \text{ arcmin}$  for the HSMEM reconstructed SZ map. This beam estimate of the reconstructed thermal SZ map has been obtained by applying a  $\chi^2$ -fit of the convolved input map to the reconstructed thermal SZ map. If we define that a cluster is convolved in the case that this FWHM radius estimate exceeds the FWHM of the reconstruction beam, which ensures that a cluster significantly contributes to several beams, a fraction of approximately 10 per cent of the recovered clusters of flux  $Y \geq 2 \times 10^{-3} \text{ arcmin}^2$  is found to be resolved.

Moreover, for comparison the expected and recovered cluster radius distributions for the cluster extent at which the change of the integrated flux with radius becomes equivalent to the contribution expected from  $3 \times \sigma_{noise}$  are shown in Figure 12. Both distributions show the same onset at low cluster radii (approximately 8 to 9 arcmin). Due to overestimation of the cluster radii by cluster-cluster confusion and noise, the distribution obtained from the reconstructed SZ map appears to be broader and less peaked. However,



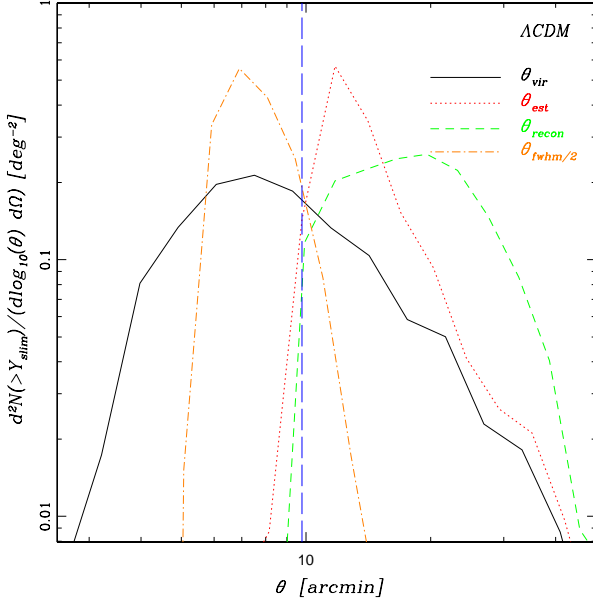


**Figure 12.** The angular size distribution of clusters in the fiducial  $\Lambda$ CDM survey with  $Y \geq 2 \times 10^{-3} \text{ arcmin}^2$ . The solid black curve represents the distribution of the virial angular radius, the orange dotted-dashed line the distribution of the radius at half the amplitude of the cluster SZ signal after a convolution with a beam of FWHM 9.7 arcmin. The distributions of the reconstructed cluster radii and the expected radius reconstructions neglecting cluster-cluster confusion are given by the green dashed and red dotted line respectively. The cluster is cut off at the radius at which the change of the integrated flux with radius falls below the contribution expected to be due to  $3 \times \sigma_{\text{noise}}$ . The blue long-dashed vertical line represents the FWHM angular extent of the beam estimate for the reconstructed map.

for large extended clusters the reconstructed distribution again approaches the estimated one and the algorithm provides thus a reasonable estimation of the cluster radii. This occasional overestimation of projected small and mid-sized cluster radii partially accounts for the upscattering of the recovered flux distribution.

#### 5.4 The reconstructed SZ power spectrum

In addition to the cluster number count, the SZ power spectrum also strongly depends on cosmology and can thus be used to constrain cosmological parameters. Therefore, it is worthwhile investigating how well the SZ power spectra of the different models can be reconstructed by the HSMEM. In Figures 13 and 14 we plot the HSMEM reconstructed SZ power spectra for each of the considered models. For comparison also the input as well as the beam-convolved SZ power spectra are shown. To obtain the beam-smoothed power spectra, a beam of FWHM of 9.7 arcmin has been assumed, since it provides the best  $\chi^2$ -fit to the reconstruction of our fiducial  $\Lambda$ CDM model. Even though the HSMEM reconstructed power spectrum is intrinsically biased (see Stolyarov et al. 2002), in the case of the fiducial  $\Lambda$ CDM model, the reconstructed SZ power spectrum agrees well with the beam-convolved input SZ power spectrum over

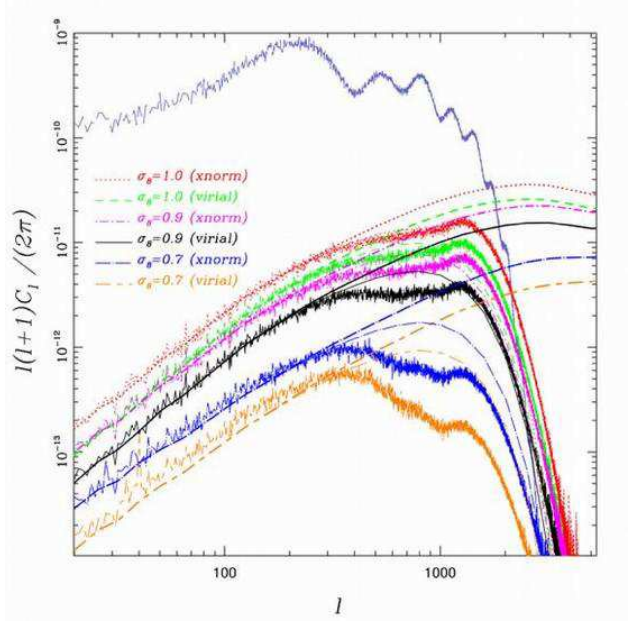


**Figure 13.** Comparison of the reconstructed thermal SZ effect power spectra in the case of the  $\Lambda$ CDM model ( $\Omega_m = 0.3$ ,  $\Lambda = 0.7$ ,  $h = 0.7$ ; Table 1) for different values of  $\sigma_8$ . The values of  $\sigma_8$ , which refer to the particular input and reconstructed power spectra, are indicated by the colour and line style. In addition we plot the input (thick lines) and beam convolved (thin lines) SZ power spectra. To obtain the beam convolved ones we assume a Gaussian beam of FWHM of 9.7 arcmin. For comparison the reconstructed primordial CMB power spectrum is also shown.

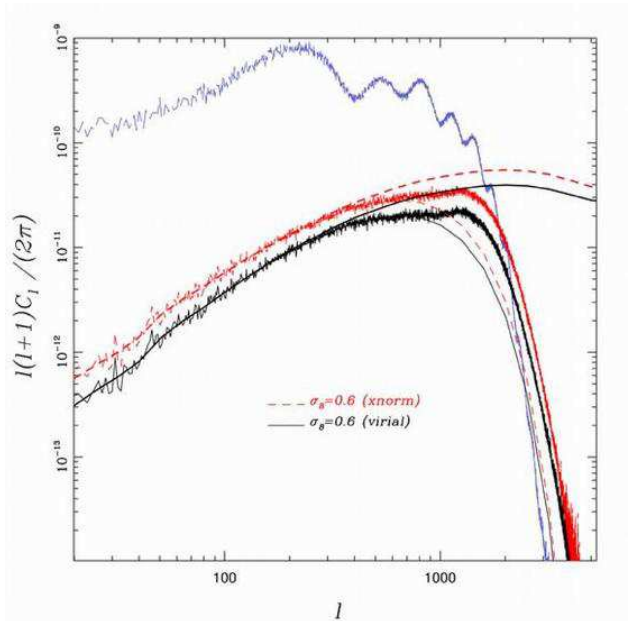


**Figure 14.** The same as 13 for the  $\tau$ CDM model ( $\Omega_m = 1$ ,  $\Lambda = 0$ ,  $h = 0.5$ ; Table 1).

a wide range of multipoles. Only on medium angular scales ( $500 < l < 1000$ ) the relative difference can be as large as 50 per cent. Nevertheless, at lower multipoles the reconstructed power spectrum is in good agreement with the corresponding true one for most of the models. Only in the case of the low- $\sigma_8$   $\Lambda$ CDM model (especially when using the virial M-T relation) the reconstructed SZ power spectrum appears to be biased. In particular, the reconstruction overpredicts the SZ power on large scales. This is due to reconstruction and residual noise of other components present in the reconstructed SZ map. Since the SZ power of the low- $\sigma_8$   $\Lambda$ CDM models is approximately an order of magnitude smaller than for the high- $\sigma_8$   $\Lambda$ CDM models, the obtained power spectra of the former models are more affected by reconstruction and residual noise. Hence, one obtains for these models an overestimated SZ power amplitude.

Furthermore, as the comparison of the beam-convolved with the reconstructed power spectrum shows, models with larger amplitudes than the fiducial  $\Lambda$ CDM model reproduce the true SZ power spectrum better at higher multipoles and seem to be less convolved. This effect arises due to the relative increase of the SZ signal in comparison to the instrumental noise and other components with fixed amplitude, such as the Galactic dust, in the high-resolution high-frequency channels of Planck. The ones with lower amplitudes show the opposite behaviour. However, up to multipoles of several hundreds the reconstructed power spectra are not significantly affected by the effective convolving beam of the reconstructed map. Thus given adequate prior knowledge about the spatial correlations of galaxy clusters, the outer cluster profile and the M-T relation, our simulations suggest that the reconstructed SZ power spectrum at low multipoles can provide constraints on cosmological parameters in addition to the cluster number count. As shown by Komatsu & Seljak (2002) the constraints on the cosmological parameters obtained by the SZ power spectrum can be used to break degeneracies between parameter constraints deduced from cluster number counts.

## 6 SUMMARY AND CONCLUSIONS

The Planck Surveyor satellite offers the opportunity to compile a large sample of galaxy clusters over the full sky. This additional aim of the Planck mission – besides determining the primordial CMB power spectrum at high angular resolution – can be a very powerful cosmological tool. We have performed full-sky multi-component simulations of future Planck SZ observations with a high degree of realism. This is the first time that on the basis of full-sky simulations and an application of a particular detection algorithm the SZ cluster gain of the Planck mission has been investigated.

Based on cluster mass and redshift catalogues obtained from N-body simulations and a mass function we derived a model sky, using further cluster properties from scaling relations. Our modelling utilised two different normalisations of the M-T scaling relation to explore the dependence of our results on its choice. The one derived from X-ray observations is more likely to include cluster physics, such as preheating and cooling, and gives a higher gas temperature for a given cluster mass. The theoretically derived one has been normalised with adiabatic hydrodynamical simulations and

presents a lower bound. To model the extent of the cluster electron gas we used the  $\beta$ -profile which is sufficient given the resolution of Planck. On the basis of this modelling we investigated the dependence of the SZ power spectra on  $\sigma_8$ . We found that the power law index  $\alpha(l)$  of the  $C_l$  dependence on  $\sigma_8$  possesses a negative slope in  $l$ -space, which we argue can explain the wide range of estimates for  $\alpha$  obtained previously by various authors. Moreover, all confusing extragalactic and Galactic components known to be significant have been incorporated in our full-sky simulations of the Planck channel detections. By the current state of art our modelling is sufficient to yield reliable results.

Further, we have applied a SZ cluster detection algorithm existing of two steps, the HSMEM to separate the SZ signal from other contaminating components and a cluster finder. In the present work the simulated performance of Planck as a SZ cluster survey instrument in combination with our detection algorithm has been tested for several models including the ones favoured by current data. On the basis of the fiducial  $\Lambda$ CDM cosmology (see Table 1) we estimated a conservative flux survey limit of  $Y = 2 \times 10^{-3} \text{ arcmin}^2$ . Given this limit a sufficient completeness and purity is obtained for the majority of the investigated models. Only in the case of the  $\sigma_8 = 0.7$   $\Lambda$ CDM model the completeness and purity have been found to be significantly lower than 80% for  $Y_{\text{surveylim}} = 2 \times 10^{-3} \text{ arcmin}^2$ . In the case that cluster contributions to a single SZ peak detection can be disentangled, it has been shown that the survey limit can be lowered to  $1 \times 10^{-3} \text{ arcmin}^2$ . Our investigations indicate that the cluster selection of the detection algorithm is non-trivial and shows a cosmological dependence mainly due to the strong cosmological variation of the SZ signal magnitude. Ideally, the cluster detection algorithm returns a cluster sample whose completeness and purity are cosmology independent, since otherwise one has to rely on prior information and mock simulations as performed in the present work. However, in practice this ideal case can hardly be reached. Nevertheless, prior constraints can be obtained from the power spectrum of the SZ effect and thus allow a self-consistent cosmological parameter estimation based on the Planck SZ detection. Therefore, as suggested by our simulations besides serving as a basis for follow-up requiring a major observational effort the recovered Planck cluster catalogue itself can already be used to put constraints on cosmological parameters. A simple conservative investigation based on our SZ detection algorithm in section 5.2 showed that a Planck SZ cluster survey will be able to distinguish between the considered vanilla models by at least a few  $\sigma$ . Given our algorithm we will investigate how tightly cosmological parameters can be constrained by a Planck SZ survey in a future paper.

Thus, as our results suggest Planck will not only be a powerful tool to constrain cosmology via primordial CMB fluctuations but will also have the ability to obtain independently constraints from the secondary effect of SZ distortions.

## 7 ACKNOWLEDGEMENTS

JG acknowledges support by an Isaac Newton Fellowship of the Isaac Newton Trust of the University of Cambridge. We

especially thank Vlad Stolyarov for providing the HSMEM code and for several helpful discussions about its application to full-sky simulations. Moreover, we acknowledge the HEALPix collaboration for providing the pixelisation scheme used in this work and the Virgo Consortium for making the Hubble Volume N-body simulations publically available.

## REFERENCES

- Allen S. W., Schmidt R. W., Fabian A. C., 2001, *MNRAS*, 328, 37
- Allen S. W., Schmidt R. W., Fabian A. C. & Ebeling H., 2003, *MNRAS*, 342, 287
- Arnaud M., Pratt G. W., Pointecouteau E., *Memorie della Societa' Astronomica Italiana, the Proceedings of the EPIC Consortium* (held on Oct 14-16, 2003 in Palermo)
- Bacon D.J., Massey R.J., Refregier A.R., Ellis R.S., 2003, *MNRAS*, 344, 673
- Bartelmann M., 2001, *A&A*, 370, 754
- Bennett C.L., et al., 2003, *ApJS*, 148, 1
- Bennett C.L., et al., 2003, *ApJS*, 148, 97
- Birkinshaw M., 1999, *Phys. Rep.*, 310, 98
- Blain A. W., Ivison R. J. & Smail I., 1998, *MNRAS*, 296L, 29B
- Bond J. R., et al., 2002, *ApJ*, submitted (astro-ph/0205386)
- Borgani S., Governato F., Wadsley J., Menci N., Tozzi P., Quinn T., Stadel J., Lake G., 2002, *MNRAS*, 336, 409
- Bouchet F.R., Gispert R., 1999, *NewA*, 4, 443
- Burigana C., Danese L., De Zotti G., Francheschini A., Mazzei P., Toffolatti L., 1997, *MNRAS*, 287, L17
- Carlstrom J.E., Holder G.P., Reese E.D., 2002, *ARAA*, 40, 643
- Challinor A., Lasenby A., 1998, *ApJ*, 499, 1
- Danese L., De Zotti G., Francheschini A., Toffolatti L., 1987, *ApJ*, 318, L15
- da Silva, A. C., Kay, S. T., Liddle, A. R., Thomas, P. A., Pearce, F. R. & Barbosa, D., 2001, *ApJL*, 561, 15
- da Silva A.C., Kay S.T., Liddle A.R., Thomas P.A., 2004, *MNRAS*, 348, 1401
- Diego J.M., Vielva P., Martinez-Gonzalez E., Silk J., Sanz J.L., 2002, *MNRAS*, 336, 1351
- Eke V. R., Cole S., Frenk C. S., 1996, *MNRAS*, 282, 263
- Eke V. R., Navarro J. F., Frenk C. S., 1998, *ApJ*, 503, 569
- Ensslin T. A., Hansen S. H., 2004 (astro-ph/0401373)
- Ettori S., Tozzi P., Borgani S., Rosati P., 2004, *A&A*, 417, 13
- Evrard A.E., et al., 2002, *ApJ*, 573, 7
- Finoguenov A., Reiprich T.H., Böhringer H., 2001, *A&A*, 368, 749
- Francheschini A., Mazzei P., De Zotti G., Danese L., 1994, *ApJ*, 427, 140
- Frenk C.S., et al., 2000 (astro-ph/0007362)
- Goldstein, et al., 2003, *ApJ*, 599, 773
- Gull S. F., Skilling J., 1990, *The MEMSYS5 User's Manual*. Maximum Entropy Data Consultants Ltd, Royston
- Haslam C.G.T., Salter C.J., Stoffel H., Wilson W.E., 1982, *A&AS*, 47, 1
- Herranz D, Sanz J.L., Barreiro R.B., Martínez-González E., 2002, *ApJ*, 580, 610
- Hobson M.P., Barreiro. R.B., Toffolatti, L., Lasenby A.N., Sanz J.L., Jones A.W., Bouchet F.R., 1999, *MNRAS*, 306, 232
- Hobson M.P., Jones A.W., Lasenby A.N., Bouchet F.R., 1998, *MNRAS*, 300, 1
- Hobson M.P., Lasenby A.N., 1998, *MNRAS*, 298, 905
- Hobson M.P., McLachlan C., 2003, *MNRAS*, 338, 765
- Hoekstra H., Yee H.K.C., Gladders, M.D., 2002, *ApJ*, 577, 595
- Holland W.S., et al. 1998, *Nature*, 392, 788
- Hu W., Kravtsov A.V., 2003, *ApJ*, 584, 702
- Jenkins A., Frenk C.S., White S.D.M., Colberg J.M., Cole S., Evrard A.E., Yoshida N., 2001, *MNRAS*, 321, 371
- Jonas J.L., Baart E.E., Nicolson G.D., 1998, *MNRAS*, 297, 977
- Kaiser, N., 1986, *MNRAS*, 222, 323
- Kay S.T., Liddle A.R., Thomas P., 2001, *MNRAS*, 325, 835
- Kneissl R., Jones M.E., Saunders R., Eke V.R., Lasenby A.N., Grainge K., Cotter G., 2001, *MNRAS*, 328, 783
- Komatsu, E. & Kitayama, T., 1999, *ApJL*, 526, L1
- Komatsu, E. & Seljak, U., 2002, *MNRAS*, 336, 1256
- Kuo C.-L., et al., 2003, *AAS*, 34, 1324
- Lacey C., Cole S., 1993, *MNRAS*, 262, 627
- Lewis A., Challinor A., Lasenby A., 2000, *ApJ*, 538, 473
- Lo K.Y., Chiueh T., Martin R.N., 2000, *AAS*, 197, 5603
- Mason B., CBI Collaboration, 2001, *AAS*, 199, 3401
- Mather J. C., Fixsen D. J., Shafer R. A., Mosier C., Wilkinson D. T., 1999, *ApJ*, 512, 511
- Mohr J. J. et al., 1995, *ApJ*, 447, 8
- Mohr J.J., Carlstrom J.E., The Sza Collaboration, 2002, *AMiBA 2001: High-Z Clusters, Missing Baryons, and CMB Polarization*, ASP Conference Proceedings, Vol. 257. Edited by Lin-Wen Chen, Chung-Pei Ma, Kin-Wang Ng, and Ue-Li Pen.
- Navarro J. F., Frenk C. S., White S. D. M., 1997, *ApJ*, 490, 493
- Pointecouteau E., Arnaud M., Kaastra J., de Plaa J., 2004, *A&A*, accepted
- Pointecouteau E., Giard M., Barret D., 1998, *A&A*, 336, 44
- Pierpaoli E., Scott D., White M., 2001, *MNRAS*, 325, 77
- Press W. H., Schechter P., 1974, *ApJ*, 187, 425
- Reich P., Reich W., 1986, *A&AS*, 63, 205
- Rephaeli Y., 1995, *ARA&A*, 33, 541
- Sadeh S., Rephaeli Y., 2004, *NewA*, 9, 373
- Sarazin C. L., 1986, *Rev. Mod. Phys.*, 58, 1
- Schlegel D.J., Finkbeiner D.P., Davis M., 1998, *ApJ*, 500, 525
- Sheth R.K., Tormen G., 1999, *MNRAS*, 308, 119
- Seljak U., Burwell J., Pen U.-L., 2001, *PhRvD*, 63, 3001
- Smail I., Ivison R. J., Blain A. W., Kneib J.-P., 1998, *AAS*, 192, 4813
- Springel, V., White, M. & Hernquist, L., 2001, *ApJ*, 549, 681
- Stolyarov V., Hobson M.P., Ashdown M.A.J., Lasenby A.N., 2002, *MNRAS*, 336, 97
- Stolyarov V., Hobson M.P., Lasenby A.N., Barreiro R.B., 2004, *MNRAS*, submitted (astro-ph/0405494)
- Sunyaev R.A., Zel'dovich Ya. B., 1972, *Comm. Astrophys. Space Phys.*, 4, 173
- Sunyaev R.A., Zel'dovich Ya. B., 1980, *ARA&A*, 18, 537
- Toffolatti L., Argüeso Gómez F., De Zotti G., Mazzei P., Francheschini A., Danese L., Burigana C., 1998, *MNRAS*, 297, 117
- White, M. 2003, *ApJ*, 597, 650
- Zhang, P.J. & Pen, U.L., 2001, *ApJ*, 549, 18